JGR Oceans

RESEARCH ARTICLE
10.1029/2018JC014730

Transport Variability of the Irminger Sea Deep Western Boundary Current From a Mooring Array

J. E. Hopkins[1], N. P. Holliday[1], D. Rayner[1], L. Houpert[1,2], I. Le Bras[3], F. Straneo[3], C. Wilson[1], and S. Bacon[1]

[1]National Oceanography Centre, Southampton, UK, [2]Scottish Association for Marine Science, Oban, UK, [3]Scripps Institution of Oceanography, University of California, San Diego, La Jolla, CA, USA

Key Points:
- Volume transport of the Deep Western Boundary Current in the Irminger Sea between 2014 and 2016 was -10.8 +/- 4.9 Sv
- Transport variability shifts from high (2-8 days) to low (55 days) frequencies with distance down slope
- No significant long-term trend in transport was identified

Correspondence to:
J. E. Hopkins,
j.hopkins@noc.ac.uk

Citation:
Hopkins, J. E., Holliday, N. P., Rayner, D., Houpert, L., Le Bras, I., Straneo, F., et al. (2019). Transport variability of the Irminger Sea Deep Western Boundary Current from a mooring array. *Journal of Geophysical Research: Oceans*, *124*. https://doi.org/10.1029/2018JC014730

Received 2 NOV 2018
Accepted 15 APR 2019
Accepted article online 23 APR 2019

Abstract The Deep Western Boundary Current in the subpolar North Atlantic is the lower limb of the Atlantic Meridional Overturning Circulation and a key component of the global climate system. Here, a mooring array deployed at 60°N in the Irminger Sea, between 2014 and 2016, provides the longest continuous record of total Deep Western Boundary Current volume transport at this latitude. The 1.8-year averaged transport of water denser than $\sigma_\theta = 27.8$ kg/m^3 was -10.8 ± 4.9 Sv (mean $\pm$ 1 std; 1 Sv $= 10^6$ m^3/s). Of this total, we find -4.1 ± 1.4 Sv within the densest layer ($\sigma_\theta > 27.88$ kg/m^3) that originated from the Denmark Strait Overflow. The lighter North East Atlantic Deep Water layer ($\sigma_\theta = 27.8$–27.88 kg/m^3) carries -6.5 ± 7.7 Sv. The variability in transport ranges between 2 and 65 days. There is a distinct shift from high to low frequency with distance from the East Greenland slope. High-frequency fluctuations (2–8 days) close to the continental slope are likely associated with topographic Rossby waves and/or cyclonic eddies. Here, perturbations in layer thickness make a significant (20–60%) contribution to transport variability. In deeper water, toward the center of the Irminger Basin, transport variance at 55 days dominates. Our results suggest that there has been a 1.8 Sv increase in total transport since 2005–2006, but this difference can be accounted for by a range of methodological and data limitation biases.

Plain Language Summary A network of currents in the Atlantic Ocean plays an important role in the global climate system, redistributing heat, salt, nutrients, and carbon around the globe. It is made up of a northward flow of warm, salty water in the upper layers of the Atlantic, and a deep, southward flow of colder, denser water. Dense water is formed at high latitudes when surface waters release heat to the atmosphere and sink toward the seafloor. This forms the Deep Western Boundary Current that moves southward to the east of Greenland. Knowing how much water is carried and whether the current is stable is vital to our understanding of global climate. Using measurements of temperature, salinity, and current speed from instruments deployed between 2014 and 2016, we find that the Deep Western Boundary Current transports on average 10.8×10^6 m^3 of water a second. This transport varies in time. It increases and decreases from day to day and month to month. Eddies, waves, and other ocean currents all contribute to these fluctuations. Our results suggest that transport has increased since 2005–2006, but it is possible to account for this change by considering the limitations of previous data sets and the methods used to calculate the transport.

1. Introduction

The Deep Western Boundary Current (DWBC) in the subpolar North Atlantic is the lower limb of the Atlantic Meridional Overturning Circulation (AMOC) and a key component of the global climate system (Intergovernmental Panel on Climate Change, 2013; Lozier et al., 2019). Water masses within the DWBC at this latitude originate from the dense northern overflows. Approximately 3 Sv of cold Denmark Strait Overflow Water (DSOW) spills over the Denmark Strait sill at the northern entrance to the Irminger Sea (B. Dickson et al., 2008; Jochumsen et al., 2017). This is joined by North East Atlantic Deep Water (NEADW), which contains modified Iceland-Scotland Overflow Water, a dense overflow that originates from the shallow sills between Iceland and Scotland (Figure 1a). Around 3 Sv of Iceland-Scotland Overflow Water is initially transported across the sill (Østerhus et al., 2008). As it makes its way around the Reykjanes Ridge and into the Irminger Basin it entrains higher salinity Atlantic water and is also influenced by some Antarctic-origin bottom waters.

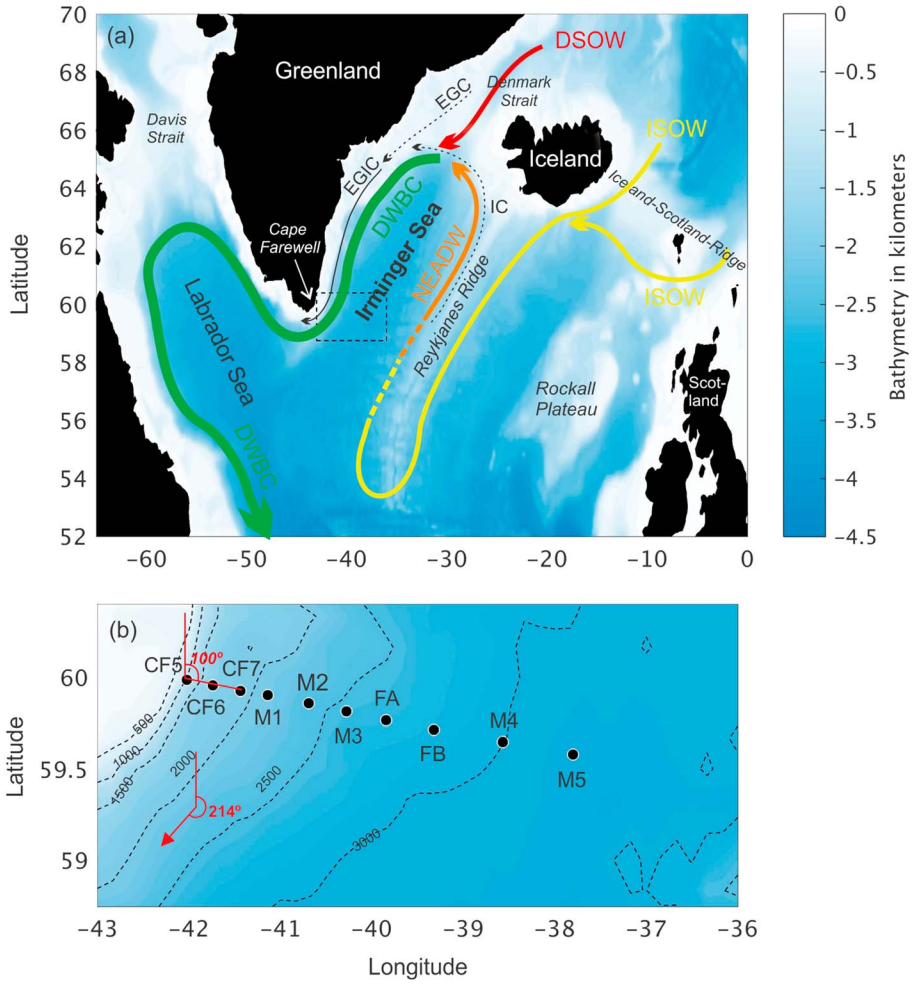

Figure 1. (a) Map of the subpolar North Atlantic schematically showing the pathway of the Deep Western Boundary Current (DWBC) and the main dense water overflows that feed into it, Denmark Strait Overflow Water (DSOW) and Iceland-Scotland Overflow Water (ISOW). ISOW is modified along its path, eventually becoming North East Atlantic Deep Water (NEADW). The shallower East Greenland Current (EGC), Irminger Current (IC), and East Greenland Irminger Current (EGIC) are also marked. Location of the Overturning in the Subpolar North Atlantic Program (OSNAP) mooring array at 60°N is marked with a dashed black box. (b) Locations of the 10 moorings. The mooring array orientation (100°) and the definition of along slope adopted here (214°) are indicated.

The DWBC flows south along the deepest reaches of the East Greenland continental slope toward Cape Farewell, the southern tip of Greenland (Figure 1a). It runs parallel to the East Greenland Irminger Current (EGIC), a slope current with a much shallower core that comprises both fresh, cold water from the Arctic carried by the East Greenland Current, and warm, saline water of Atlantic origin transported by the Irminger Current (Bacon et al., 2002; Daniault et al., 2011; Le Bras et al., 2018).

After the DWBC passes Cape Farewell, it circulates around the Labrador Sea and crosses into the subtropical North Atlantic along the western boundary of the North American continent, eventually becoming North Atlantic Deep Water, a water mass that constitutes a significant fraction of the world's oceans (Johnson, 2008). Along its path it is continuously modified, most notably by the addition of Labrador Sea Water (LSW), the product of cumulative deep convection events within the Labrador Sea, Irminger Basin, and more widely across the North Atlantic Subpolar Gyre (Pickart et al., 2003; Rhein et al., 2015).

Although models suggest that AMOC variability is linked to deep water formation over the subpolar North Atlantic (Danabasoglu et al., 2016; Stouffer et al., 2006), implying that AMOC variability should be reflected in DWBC transport and properties, there is no conclusive observational evidence to

support this (Lozier, 2012; Schott et al., 2004; Straneo, 2006; Toole et al., 2017). It is likely that alternative pathways linking the basin interior and boundary currents, recirculation cells, the strength of the eddy field, and variability in the wind stress all play a role in modifying the transport of the DWBC and its linkage with the AMOC (Bower et al., 2009; Holliday et al., 2007; Lavender et al., 2000; Le Bras et al., 2017; Peña-Molino et al., 2012).

Various estimates of DWBC transport have been made between Denmark Strait at 67°N and the Grand Banks at 45°N (B. Dickson et al., 2008; R. R. Dickson & Brown, 1994; Kieke & Rhein, 2006; Mertens et al., 2014; Zantopp et al., 2017). Here we focus on the DWBC as it passes Cape Farewell at a latitude of 60°N. Only a handful of total transport estimates from mooring arrays have been made in this region. Combining a hydrographic section with a 60-day deployment of current meters in 1978 Clarke (1984) calculated a total volume transport of 13 Sv for water denser than $\sigma_\theta = 27.8$ kg/m^3. Using a 9.5-month record from a mooring array deployed 27 years later, in 2005–2006, Bacon and Saunders (2010) calculated the mean total transport to be 9 Sv (for $\sigma_\theta > 27.8$ kg/m^3), with a range of 0–16 Sv. They also argued that the earlier 13 Sv from Clarke (1984) was more likely to have been 16 Sv and conclude that there had been a significant weakening of the total DWBC transport since 1978.

Other estimates have been made from either "snapshot" or repeated summertime hydrographic sections at 60°N (Bacon, 1997; Bersch, 1995; Daniault et al., 2016; R. R. Dickson & Brown, 1994; Holliday et al., 2009; Holliday et al., 2018; Lherminier et al., 2007; Lherminier et al., 2010; Sarafanov et al., 2012; Vage et al., 2011). They provide a range of transport estimates between 5.5 and 13.3 Sv (for water denser than 27.8 kg/m^3, or comparable threshold of $\sigma_2 < 36.94$).

Decadal scale variability of the baroclinic transport at 60°N has been identified in a number of studies where baroclinic geostrophic velocities have been derived from repeat hydrography and referenced to levels of no motion at intermediate water depths (Bacon, 1998; Kieke & Rhein, 2006; Sarafanov et al., 2009). Transport was low in the 1950s and 1960s, high in the late 1970s and early 1980s, low again in the early to mid-1990s and increased to a moderately high state in the 2000s. Sarafanov et al. (2009) report decadal scale baroclinic transport variability of 2–2.5 Sv between 1955 and 2007. These estimates, however, are unable to account for changes in the absolute velocity at the reference level and so may lead to underestimate or overestimate of the total transport (Sarafanov et al., 2010). A sparsity of sustained direct velocity measurements over decadal time scales prevents us from conclusively knowing whether longer time scale patterns of baroclinic transport are reflected in the total flow variability. The presence of eddies, variable entrainment rates, strengthening or weakening of gyre scale circulations, and/or short-term variability that cannot be resolved during a hydrographic section can all affect calculation of the baroclinic transport and also obscure any correlation between the baroclinic and barotropic components (Kieke & Rhein, 2006). Analysis of deep velocity records obtained between 67°N and 45°N reveals a broad range of variability and strong intraseasonal signals that may mask longer-term trends (Fischer et al., 2015).

Overall, we lack an understanding of the temporal variability in total DWBC transport and its constituent water masses, particularly before it is modified by processes in the Labrador Sea. Variability exists from days to decades, due to external forcing and nonlinear processes, but so far there has been no systematic study to examine the nature of this variability. In this paper we use almost two years' worth (2014–2016) of data collected from a mooring array at 60°N, deployed as part of the transbasin array of the Overturning in the Subpolar North Atlantic Program (OSNAP; Lozier et al., 2016) to address some of these gaps in our knowledge. We pose the following questions:

- What does the mean structure of the DWBC velocity field look like and what is the total volume transport within it, decomposed into the contributions made within the DSOW and NEADW layers?
- What are the dominant time scales and magnitudes of DWBC transport variability, within a daily to seasonal frequency range?
- What contribution does eddy volume transport make?

We will compare the transport calculated from this new time series to previous estimates and consider whether apparent long-term change over time can be believed by quantifying a range of biases introduced by methodological approaches, a fixed density field, and variable record lengths.

2. Mooring Array Design, Data Collection, and Processing

2.1. Mooring Array and Instrumentation

As part of the OSNAP transbasin array (Lozier et al., 2016), the Irminger Sea DWBC array was deployed in 2014. The array was constructed of five U.K. OSNAP moorings (M1 to M5), two U.S. Ocean Observatories Initiative (OOI) flanking moorings (FA and FB), and three U.S. OSNAP East Greenland Current array moorings (CF5, CF6, and CF7; Figure 1b). The full array was in the water for 22 months (659 days), between 18 September 2014 and 8 July 2016 (see Table A1). Reference to deployment-mean quantities throughout this paper will refer to the entire 659 days (1.8 years). The deployment, servicing, and recovery of these moorings was an effort shared jointly between the National Oceanography Centre (NOC, U.K. OSNAP), the OOI, Woods Hole Oceanographic Institution (U.S. OSNAP), the Scottish Association for Marine Science, and the Netherlands Institute for Sea Research (NIOZ). There were two periods of time within which the full instrument array was in the water, referred to here as the 2014 deployment (18 September 2014 to 17 July 2015) and the 2015 deployment (22 August 2015 to 8 July 2016).

The mooring layout and nominal instrument placement is presented in Figures 1b and 2. We measure distance along the array from the location of the 50-m isobath on the East Greenland shelf. Moving offshore the moorings are spaced 16 km (CF5-CF6), 17 km (CF6-CF7), 17 km (CF7-M1), 26 km (M1-M2), 24 km (M2-M3), 25 km (M3-FA), 30 km (FA-FB), 43 km (FB-M4), and 44 km (M4-M5) apart. The moorings were deployed in a line rotated 100° from north (Figure 1b), approximately perpendicular to the isobaths of the upper (500–1,000 m) continental slope.

From the 10 moorings, we use 49 CTDs (conductivity-temperature-depth), 24 current meters, and 5 acoustic Doppler current profilers (ADCPs; see Tables A2 and A3). Given our focus on the deep boundary current, with the exception of CTDs at 750 m on moorings CF5, CF6, CF7, and M1, we only use instrumentation deployed at or deeper than 1,000 m. The CTDs were vertically spaced by a minimum of 145 m and a maximum of 500 m. Their average vertical spacing was 316 m. The current meters and ADCPs were on average 423 m apart, with minimum and maximum vertical separations of 266 and 725 m, respectively.

Conductivity, temperature, and pressure were recorded by SBE37 MicroCATs on all moorings. Sampling intervals varied between 7.5 min and 1 hr. The sampling intervals for the current meters were either 30 or 60 min. Tables A2 and A3 provide details on individual instrument setups. All five 300-kHz RDI ADCPs were mounted in a downward looking configuration close to the seafloor. They recorded velocities every hour in 4-m bins over a 104-m depth range.

Overall, the quantity and quality of data recorded by instrumentation were excellent. Only a small number of the MicroCATs returned unusable data. The temperature and salinity records from the instrument nominally at 2,100 m deployed on mooring FA in 2015 suffered from unrecoverable drift and significant jumps so were discarded. The conductivity and salinity from 1,955 m on M1 between 20 January and 23 July 2015 were also unusable. The ADCP deployed at M4 in 2014 failed and returned no useable data, although we have been able to estimate the velocities at this location (see Appendix A1). The quality of data recorded by the ADCPs on the NOC moorings (M1 to M5) became increasingly degraded in the spring. This is thought to be caused by a reduction in the number of scatterers in the water column. Throughout each deployment the range (the distance from the transducer head to the last useable bin) over which good quality data were returned reduced from 60–100 to 20–40 m. Other shorter gaps, for example, where the conductivity cell on the CTDs appeared temporarily blocked, or gaps introduced during mooring servicing (Table A1) were filled (see Appendix A1 for details).

2.2. Processing of Moored CTD and Current Meter Data

Predeployment and postdeployment manufacturer calibrations were used to assess and correct any offsets and drift in the SBE37 MicroCAT data. Additional calibration was applied to the 26 NOC and 11 U.S. MicroCATS. While on station, during both the deployment and recovery cruises (recovery only for the U.S. instruments), the MicroCATs were strapped to the CTD frame. Where stops were made to collect water samples on the up-casts comparisons were made between the pressure, temperature, and conductivity of the CTD and the corresponding MicroCAT measurements. These were used to correct for any offset and drift that may have occurred during the deployment.

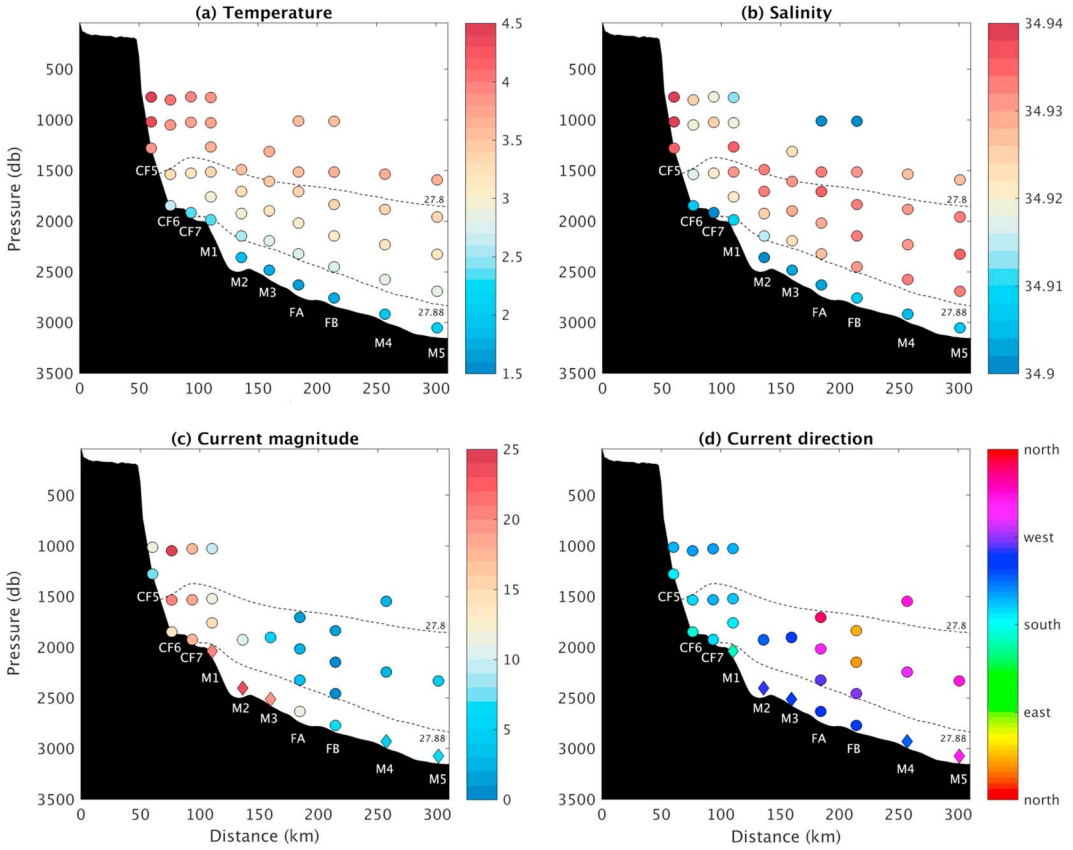

Figure 2. Deployment-mean (a) temperature (°C) and (b) salinity at each of the nominal conductivity-temperature-depth locations on moorings CF5 to M5. (c) Deployment-mean current magnitude (cm/s) and (d) direction from each nominal current meter location (circles) and the deepest useable bin from the acoustic Doppler current profilers (diamonds). Pressures are the deployment means. The dashed lines mark the deployment mean 27.8- and 27.88-kg/m^3 isopycnal depths calculated in this study.

All current meters were corrected for magnetic declination (typically around −21°). Additionally, the speed of sound parameters set before deployment was checked against colocated CTD data and corrected if necessary. Spikes in temperature, salinity, pressure, and velocity were removed and each variable regridded onto 1-hr time stamps using linear interpolation. A 40-hr low-pass filter was run to remove any tidal and near-inertial oscillations. Finally, 12-hr averages, centered around midday and midnight, were created.

2.3. CTD and LADCP Data

Our moored observations are supported by four hydrographic and lowered ADCP (LADCP) sections completed along the mooring array between 2014 and 2016, and a further two sections completed in 2005 and 2008 slightly further south. Research cruises onboard the RRS James Clark Ross (JR302) and the RV Knorr (KN221) both completed sections in June 2014 and August 2014, respectively. In July 2015 the Netherlands Institute for Sea Research carried out a hydrographic survey onboard the RV Pelagia (PE400) in support of the OSNAP and NACLIM research programs. A fourth section was completed in August 2016 by the RRS Discovery (DY054) as part of the U.K. OSNAP cruise program. The 2005 and 2008 sections were both completed in September from the RRS Discovery (cruises D298 and D332 respectively) in the vicinity of the WOCE (World Ocean Circulation Experiment) hydrographic section AR7. Synoptic snapshots of the velocity and density fields from the CTD and LADCP sections allow us to validate our interpolation.

3. Velocity Variance and Decorrelation Length Scales

Before proceeding with a calculation of the volume transport within the DWBC, we first examine the characteristics of the velocity field. This informs our definition of along-slope velocity and provides information on decorrelation length scales that are relevant to our interpolation scheme (section 4).

3.1. Mean Current Speed and Direction

The deployment-mean current magnitude and direction recorded at each nominal current meter location on the array is shown in Figure 2. In Figure 3 the mean currents recorded from each near bed current meter and the nearest instrument above it are presented (separately for the 2014 and 2015 deployments). Nearest the seabed, the mean current speed increases from 7 cm/s at CF5 to a maximum of 23 cm/s at M2. It then decreases steadily toward a minimum of 5 cm/s at mooring M4. Offshore of CF7 the current magnitude decreases with height above the bottom. Between CF5 and CF7 however the current speed increases away from the seafloor (Figures 2c and 3a).

Away from the seabed, maximum southward currents (>20 cm/s) are found at CF6. These reduce rapidly toward the interior of the basin (Figure 2c). East of mooring M3 there are weak (<10 cm/s) northwest to northeast flows between 1,500- and 2.500-m depths (Figure 2d). Moorings M1 and M2 are separated by a steep bathymetric slope. There is a distinct transition from southward currents between CF5 and M1 on the upper, western side of this rise to a more southwesterly mean flow near the bottom in deeper water between M2 and M4. At M5 there is a weak northwesterly near bed mean flow (Figures 2d and 3b).

3.2. Variance Ellipses

Between CF5 and FA the orientation of the major axis of the deepest variance ellipses all align with the local, upstream bathymetry contours (central map in Figure 4), consistent with a bathymetrically steered current. Topographic control is strongest at CF5 where the variance ellipse tightly bounds the two-dimensional velocity histogram and is oriented close to the direction of the mean current (Figure 4a). Moving offshore between CF5 and CF7, the mean current direction becomes increasingly offset from the ellipse major axis.

Moorings M1 and M2 look to have been deployed across a local indentation in the continental slope that is oriented approximately northwest to southeast. This accounts for the steep bathymetric rise between these two moorings and for the almost 90° difference in both the mean current direction and ellipse orientation of the bottom velocity records (Figures 4d and 4e). Slightly higher in the water column the orientation of the variance ellipses at M1 and M2 are more comparable and match more closely the velocity record from neighboring moorings (not shown).

The variance ellipses become increasingly isotropic with distance downslope. In deeper water (at FB, M4 and M5) the major axis of velocity variance is oriented approximately northwest to southeast, close to the orientation of the mooring array, meaning that greater velocity variability is felt across isobaths than along them (Figures 4h–4j and Figure 4 central map). Eastward of M2 the two-dimensional histograms reveal increasingly sinuous and less coherent velocity traces.

3.3. Decorrelation Length Scales

An assessment of whether the mooring spacing and instrument placement is able to resolve the dynamics of the velocity and density fields within the DWBC can be made by evaluating the vertical and horizontal decorrelation length scales (r_v and r_h) of the velocity, temperature and salinity (see Appendix A2 and Figure A2 for details of this calculation). This also helps determine the appropriate horizontal and vertical length scales for the weighting function used in the interpolation scheme (see section 4).

Temperature observations become decorrelated at a separation distance of between 39 and 45 km (Table 1 and Figure A2a). Measurements of salinity become decorrelated over slightly shorter distances, 32–36 km (Figure A2c). The horizontal decorrelation length scales of temperature and salinity are therefore about twice the average of mooring separation distances between CF5 and FA. Vertically, the decorrelation length scale of temperature (517–600 m) is double the average vertical separation of CTDs (316 m; Figure A2b). The vertical salinity decorrelation is 295–321 m (Figure A2d) indicating that vertical variability in the salinity field is only just resolved at each mooring.

The along-slope velocity becomes decorrelated over a distance of 18–24 km in the horizontal (Figure A2e). This is about twice the local baroclinic Rossby Radius, estimated to be 10 km (Chelton et al., 1998). The horizontal scale of the flow is therefore only just resolved between the first three moorings (CF5, CF6, and CF7) that are spaced 16–17 km apart. Beyond CF7 the distance between the moorings increases from 26 to 44 km, and neighboring velocity records are no longer coherent. The station spacing on the far eastern

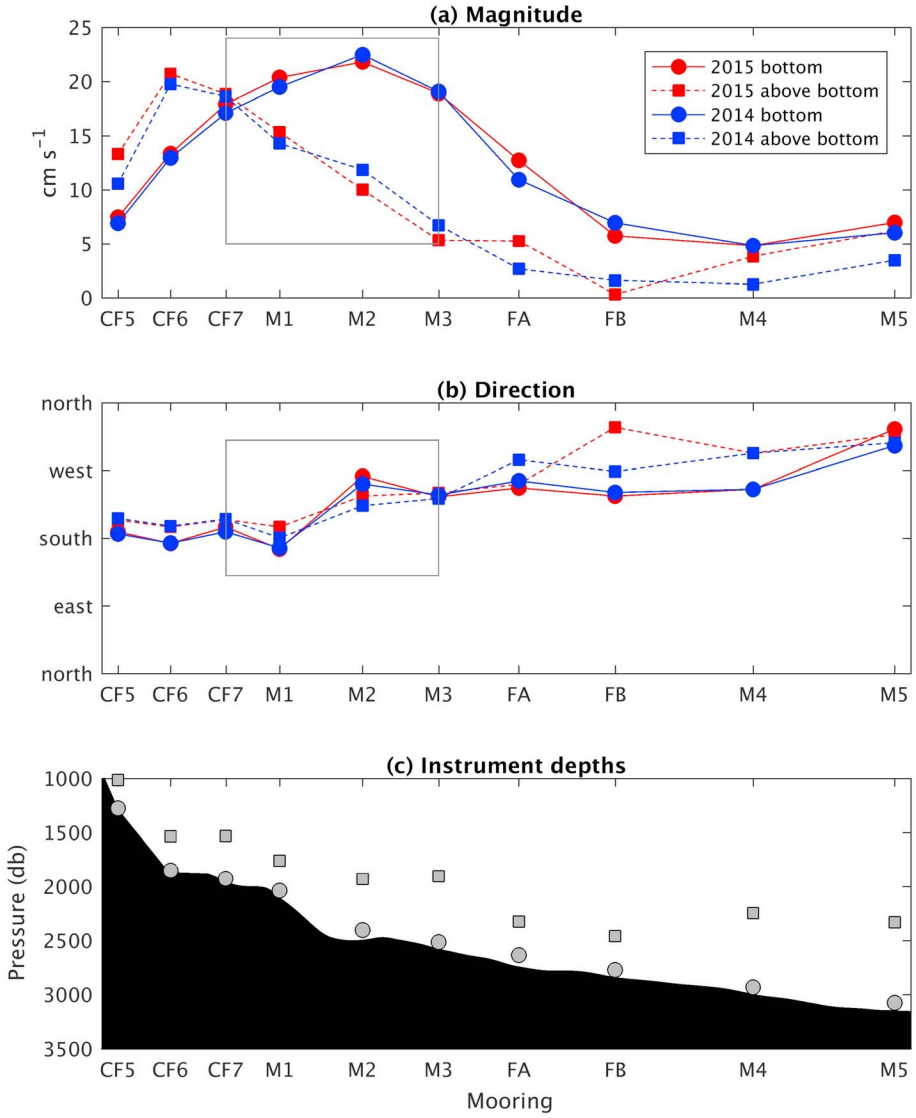

Figure 3. (a) Mean current magnitude and (b) direction during the 2014 (blue) and 2015 (red) deployments. Solid lines (circles) are for the current meters nearest the sea floor. Dashed lines (squares) are the nearest instrument above. The gray box indicates the moorings over which the mean current direction, subsequently used to define the along-slope velocity component, was calculated. (c) Deployment mean depths of the current meters used in (a) and (b).

side of the array is therefore unable to fully resolve the smaller-scale flow dynamics. The vertical decorrelation length scales are large (1,478–1,867 m) reflecting the barotropic nature of the observed flow below 1,000 m (Figure A2f).

4. Calculating the DWBC Transport

Our primary objective is to calculate the volume transport within the DWBC of the Irminger Sea. The temporal and spatial coverage of instrumentation within our array (Figure 2 and Tables A1, A2, A3) is sufficient to allow interpolation of the density and velocity fields onto a regular grid. Integration of the along-slope component of flow (that crosses the mooring array) within density classes is then easily performed to obtain transports. In line with Dickson and Brown (1994) and Holliday et al. (2009) we define water with a potential density greater than $\sigma_\theta = 27.8$ kg/m^3 as being part of the DWBC. The boundary separating DSOW from overlying NEADW is less consistent between authors. Here, following Holliday et al. (2009), we define NEADW

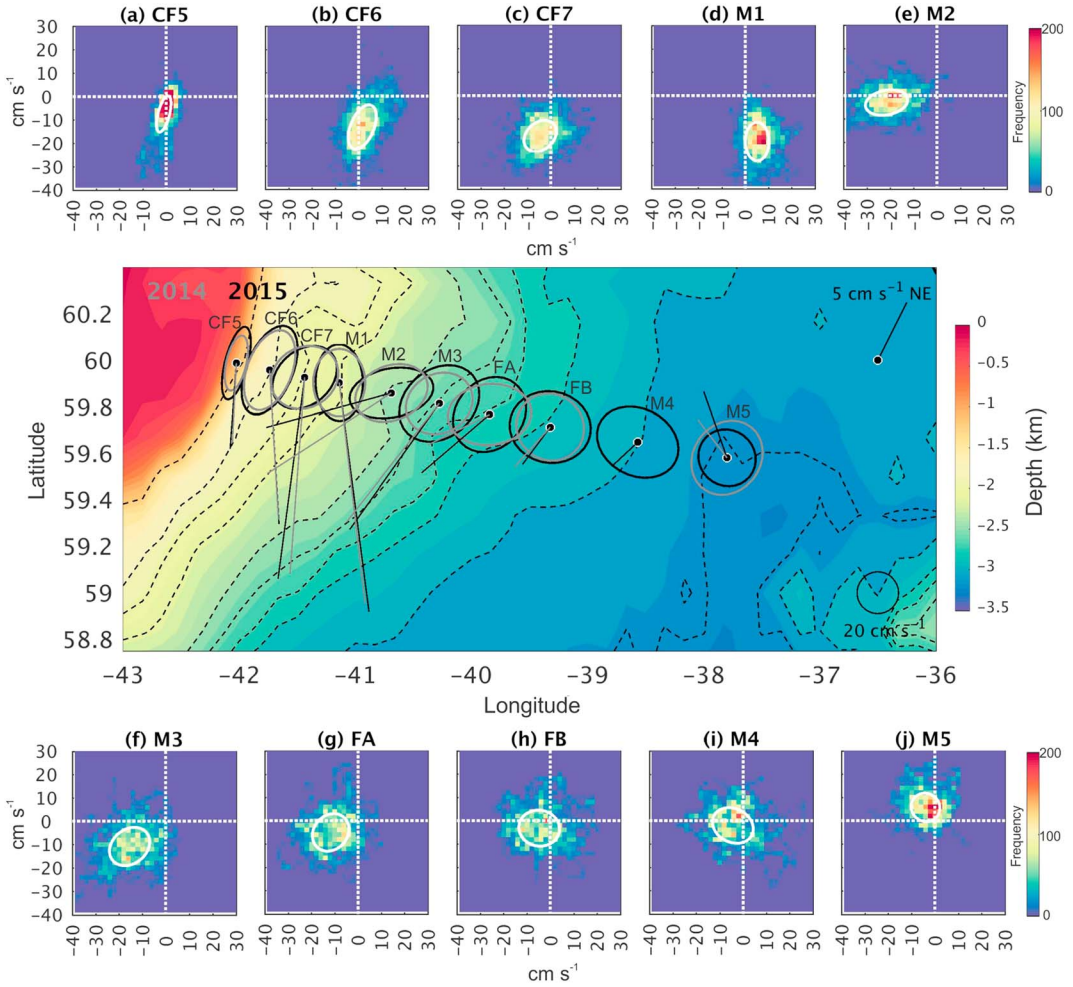

Figure 4. (central map) Variance ellipses for the near-bed velocity records during the 2014 (gray) and 2015 (black) deployments. Sticks represent the deployment mean velocity vectors. Bathymetry contours are marked at each of the mooring depths. (a–j) Two-dimensional histograms of near-bed low-pass-filtered velocity records during the 2015 deployment. Variance ellipses overlaid in white.

as lying in the potential density range $\sigma_\theta = 27.8$–27.88 kg/m^3, the lighter isopycnals representing the Iceland-Scotland Overflow contribution. We define DSOW as having $\sigma_\theta > 27.88$ kg/m^3.

In this section, we describe the interpolation scheme that we use to produce 12-hourly fields, justify our choice of weighting parameters, and validate the results using independent hydrographic sections and statistical metrics.

Table 1
Vertical and Horizontal Decorrelation Length Scales (r_v and r_h, respectively) and the Horizontal and Vertical Standard Deviations (σ_x,σ_z) used in the Interpolation

Variable	r_h (km)	r_v (m)	σ_x (km)	σ_z (m)	$xr_{\max}$ (km)	$zr_{\max}$ (m)
Temperature	39–45	517–600	$20 + 10\tanh\left(\frac{x-115}{35}\right)$	200	50	400
Salinity	32–36	295–321	$20 + 10\tanh\left(\frac{x-115}{35}\right)$	200	50	400
Along-slope velocity	18–24	1,478–1,867	$16 + 6\tanh\left(\frac{x-100}{15}\right)$	200	40	400

Note. $xr_{\max}$ and $zr_{\max}$ are the maximum horizontal and vertical search radii.

4.1. Interpolation Scheme

Observations always contain errors (e.g., instrument accuracy, synopticity, or calibration errors). We have therefore produced a "field approximation" rather than a strict (e.g., linear or cubic) interpolation where observational noise and error tend to be amplified. The velocity, temperature, and salinity time series were interpolated onto an equidistant grid with cell sizes of 10 m vertically and 1 km horizontally. We use an iterative objective analysis approach (Barnes, 1964, 1973) that seeks to produce a smooth field that reproduces within it the observations as closely as possible. This technique is suitable for an unstructured but reasonably uniformly distributed set of observations.

For any given grid point i, j, the interpolated function $g(x_i,z_j)$ is first approximated from an inverse weighting of the data points. A two-dimensional Gaussian weighting function with different horizontal and vertical scales is used such that at point i, j the weightings assigned to each of the n observed values at locations (x,z) are given by

$$w_{ij} = \exp\left(-\frac{(x-x_i)^2}{{\sigma_x}^2}-\frac{(z-z_j)^2}{{\sigma_z}^2}\right) \tag{1}$$

The variance in the horizontal (${\sigma_x}^2$) and vertical (${\sigma_z}^2$) dimensions respectively determine the horizontal (distance along the array) and vertical (depth) widths of the Gaussian function. The initial (first guess) interpolation $g_0(x_i,z_j)$ at grid point i, j from the n observed values $f_n(x,z)$ is then

$$g_0(x_i,z_j)=\frac{\sum_n w_{ij} f_n(x,z)}{\sum_n w_{ij}} \tag{2}$$

During the next iteration, the difference between the observed field and the interpolated values at the measurement points is used to optimize the result. The first correction $g_1(x_i,z_j)$ to the initial interpolation is given by

$$g_1(x_i,z_j) = g_0(x_i,z_j) + \frac{\sum_n w_{ij}(f_n(x,z)-g_0(x,z))}{\sum_n w_{ij}} \tag{3}$$

where $g_0(x,z)$ is the value of the interpolated function at the n measurement points (x,z). Successive correction steps producing $g_2(x_i,z_j)$, $g_3(x_i,z_j)$ ... etc. can then be used in order to achieve better agreement between the interpolated function and the measured values. Two adjustment iterations were used here (up to $g_2(x_i,z_j)$).

This iterative correction method is appealing for a number of reasons. First, no a priori knowledge is required about the field variable. The observations themselves provide the initial guess. Second, mooring knockdown (up to 250 m) and the resulting variability in the pressure record is accounted for; that is, we do not assume fixed depths for each instrument. Third, when appropriate values of σ_x and σ_z are chosen, the smoothly varying field that is produced does not contain any unphysical discontinuities.

The decorrelation length scales (Table 1) are used to guide our choice of σ_x and σ_z. The value of σ_x needs to be one that maximizes the horizontal resolution of the narrow EGIC that follows the continental slope between CF5 and CF7 and also accounts for the increasing distance between moorings along the array. Reducing σ_x brings the interpolated value at each instrument location closer to the observed value, but this creates unphysical transitions in temperature, salinity, and velocity between moorings on the eastern side of the array that are located further apart. A compromise is therefore necessary.

Rather than set a fixed value, we allow σ_x to increase as a function of distance along the array, from 10 km at the wall of the continental slope up to a distance comparable to the horizontal decorrelation length scale: 22 km for velocity and 30 km for temperature and salinity. Note that a spatially variable weighting is not strictly accounted for in the original formulation of this objective analysis technique (Barnes, 1964, 1973)

but helps improve our final product. The increase in σ_x is set by a hyperbolic tangent function centered between CF7 and M1 (see Table 1).

The vertical standard deviation of the Gaussian weighting function (σ_z) applied to the temperature, salinity, and velocity fields is set to a constant value of 200 m. We also prescribe a maximum search radius, with horizontal (xr_{max}) and vertical (zr_{max}) length scales appropriate for the instrument separations and decorrelation scales, such that only observations within xr_{max} kilometers and zr_{max} meters of the interpolated value at x_i, z_j carry any weight (see Table 1). Justification that the function we use to define σ_x provides an appropriate horizontal decay in weightings for observations of velocity is provided in Figure A3.

All direct (low-pass filtered and 12 hr averaged) observations of temperature and salinity from the 49 CTDs, and velocities from the 24 current meters are used in the interpolation. From each of the five ADCPs we use the velocity record from the deepest reliable bin. At each 12-hr time step, before the Barnes optimal interpolation, we perform a set of much simpler linear extrapolations to (a) help maximize the area over which an optimally interpolated field could be generated, (b) to force a more physical structure within the DWBC itself, and (c) to improve the optimal interpolation near regions of steep topography. Further details are provided in the appendix.

We wish to compute a volume transport that best represents the contribution made by the DWBC in the Irminger Sea to the AMOC. Figures 2–4 all demonstrate that the magnitude, direction, and major axes of velocity variance are strongly dependent upon the local bathymetry, water depth, and height above the seafloor. The strongest near bottom currents are found between moorings CF7 and M3 (16–23 cm/s; gray box in Figure 3a) and are on average directed toward the southwest, 214° (gray box in Figure 3b). Based on this analysis east-west and north-south velocities were rotated 34° clockwise and replaced by components in the across-slope and along-slope directions, respectively. Negative along-slope velocities represent an equatorward current. Negative across-slope velocities represent upslope flow. The impact that this choice has on the estimated transport will be discussed in section 6. Note that we are careful to report only the along-slope component of transport that is normal to the mooring line.

4.2. Validation of Interpolation

Before deriving the volume transport, we first validate the results of our interpolation and present the deployment-mean water masses and velocity structures that are resolved within the western Irminger Basin by the OSNAP mooring array.

4.2.1. Observation-Interpolation Statistics

The performance of the interpolation is assessed by calculating the root-mean-square deviation (rmsd) between the observations made by each instrument and the time series of interpolated values at the matching locations. Figures 5a and 5b present the rmsd for the temperatures and salinities recorded by the 49 CTDs within the mooring array. The rmsd of along-slope velocity at the 24 current meters and 5 ADCPs is shown in Figure 5c. The rmsd averaged across all instruments is reported in Table A4.

Averaged across all instruments the rmsd for salinity is 0.003 ± 0.002 psu (mean ± 1 std). Across the whole deployment, the interpolation is biased 6×10^{-4} psu too low (too fresh). To place this into context, the stated accuracy of the SeaBird conductivity cell is 0.003 mS/cm, which at 2.5 °C and 2,000 db equates to a salinity of 0.0036 psu. Additionally, the NOC CTDs were all calibrated following the same methods as those used for instrumentation on the RAPID mooring array, where the accuracy of salinity was reported to be 0.003 psu (McCarthy et al., 2015). The interpolation error in salinity is therefore acceptable.

The average rmsd for temperature is 0.04 ± 0.03 °C (mean ± 1 std) and the bias is 0.02 °C (too cold). These numbers are an order of magnitude greater than the accuracy of the SeaBird temperature sensor. They are, however, less than the standard deviation in temperature observed by any of the CTDs (that range from a minimum of 0.05 °C to a maximum of 0.29 °C). The bias is less than 0.5% of the range in temperature observed across the whole array.

The rmsd for along-slope velocity is 1.4 ± 0.9 cm/s (mean ± 1 std). Averaged across all instrumentation and the entire time series the interpolation is biased 0.17 cm/s too slow. The stated accuracy of the Nortek

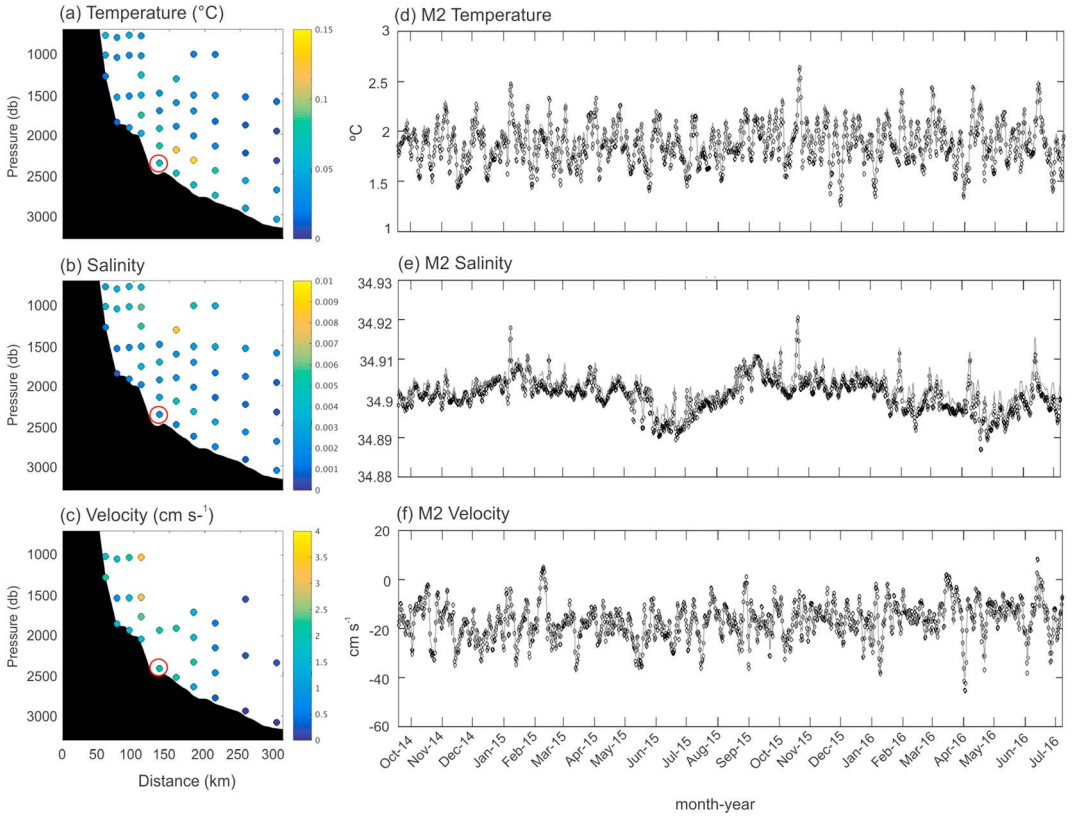

Figure 5. Root-mean-squared deviation between interpolated and observed values of (a) temperature, (b) salinity, and (c) along-slope velocity. Panels (d) to (f) show the 12-hr time series of each observed (black dots) and interpolated (gray line) variable for the deepest CTD and current meter on mooring M2 (red circles in a–c). CTD = temperature-conductivity-depth.

current meters is 1% of the measurement value ±0.5 cm/s. Within the core of the DWBC where velocities reach 20 cm/s this equates to an error of 0.2 ± 0.5 cm/s, greater than the rmsd and interpolation bias. Furthermore, the minimum and maximum standard deviations of observed along-slope velocity are 6.5 and 10.7 cm/s, respectively, both much greater than the rmsd and bias that result from our interpolation.

Time series directly comparing the interpolated and observed temperature, salinity, and along-slope velocity (Figures 5d–5f) from the deepest CTD and current meter on mooring M2 (within the core of the DWBC) visually demonstrates how well temporal variability in each of the variables is replicated.

4.2.2. Water Mass Identification and Mean Velocity Structure

The deployment-mean potential temperature, salinity, along-slope, and across-slope velocity fields from the mooring array are presented in Figure 6. All the expected major water masses and velocity structures are resolved.

Cold ($\theta < 2.2$ °C) and relatively fresh water originating from the Denmark Strait Overflow ($\sigma_\theta > 27.88$ kg/m^3) occupies a 300-m-thick layer across the deepest (>2,000 m) part of the western Irminger Basin. Warmer ($\theta = 2.2$–3.3 °C) and more saline NEADW lies above and is present further up the continental slope (up to 1,500-m depth; Figure 6a). These waters acquire their high salinity near the Iceland-Scotland sills through entrainment of Atlantic origin waters.

On the western boundary of the array the deep reaching warm and saline signature of Atlantic water carried within the EGIC, the upper portion of the equatorward Western Boundary flow is resolved, penetrating to 1,500 m (Figures 6a and 6b). The dominant intermediate water mass in the Irminger Sea is LSW. It is identifiable by the low salinities between 1,000 and 1,500 m over the central parts of the basin (Figures 6b, 7c, and 7d).

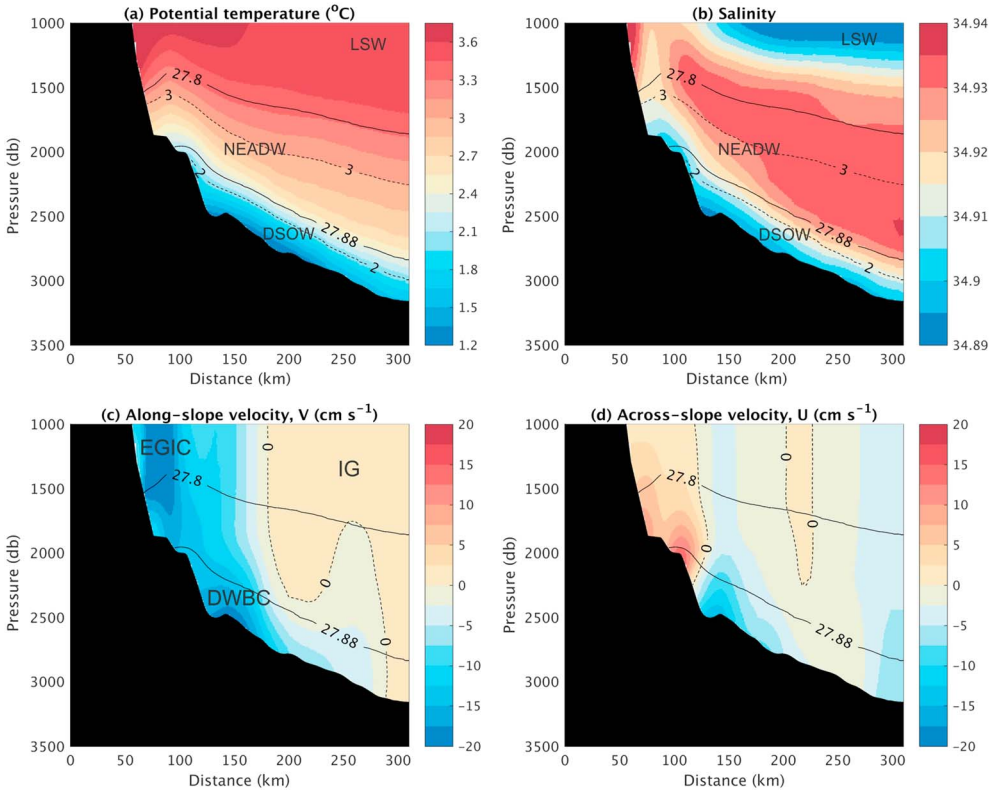

Figure 6. Deployment-mean (a) potential temperature (°C), (b) salinity, (c) along-slope (cm/s), and (d) across-slope velocity (cm/s) calculated from 12-hourly sampled time series. Solid black contours in each panel mark the deployment mean potential densities of 27.8 and 27.88 kg/m^3. Dashed contours in (a) and (b) are the deployment mean potential temperatures of 3 and 2 °C. Labrador Sea Water (LSW), North East Atlantic Deep Water (NEADW), Denmark Strait Overflow Water (DSOW), the East Greenland Current (EGIC), the Irminger Gyre (IG), and the Deep Western Boundary Current (DWBC) are identified.

Westward of the 3,000-m isobath there is unidirectional equatorward flow between the seafloor and 1,000 m (Figure 6c). Within this flow field two distinct velocity cores are identified. The first, between 1,000- and 1,500-m depths immediately seaward of the continental slope (>20 cm/s), is the surface intensified but deep reaching EGIC. The maximum velocity appears to shift slightly eastward as it approaches the bottom, consistent with LADCP sections presented in Daniault et al. (2011). The second, in 2,500-m water depth approximately 150 km along the mooring array, is the 50-km-wide DWBC velocity core (15–20 cm/s). Its tail extends downslope toward the center of the Irminger Basin to just over 3,000-m depth. Its width and velocity gradually decreases.

At 250 km along the array, at the tail end of the weakening southward flow, there is a pronounced thickening of the deep boundary current. Here, negative velocities extend from the seafloor up to the 27.8-kg/m^3 isopycnal. A similar, midbasin southward flow, isolated below the 27.8-kg/m^3 isopycnal was observed in Holliday et al. (2018).

A region of weak (<5 cm/s) poleward flow to the east of our section is the northward branch of the Irminger Gyre cyclonic recirculation and is consistent with both observational and modeling studies (Kase et al., 2001; Lavender et al., 2000; Vage et al., 2011). Immediately upslope of the DWBC velocity core the mean cross-slope velocities are convergent (Figure 6d), consistent with Figure 4.

4.2.3. Comparison to LADCP and CTD Sections

The temperature, salinity, and density structures resolved by the mooring array during cruise PE400 in July 2015 compare well to the ship's hydrographic section (Figures 7a–7d). The CTD section from the RV Pelagia was completed between the 17 and 25 July 2015. Therefore, in addition to the average depth of the 27.8- and

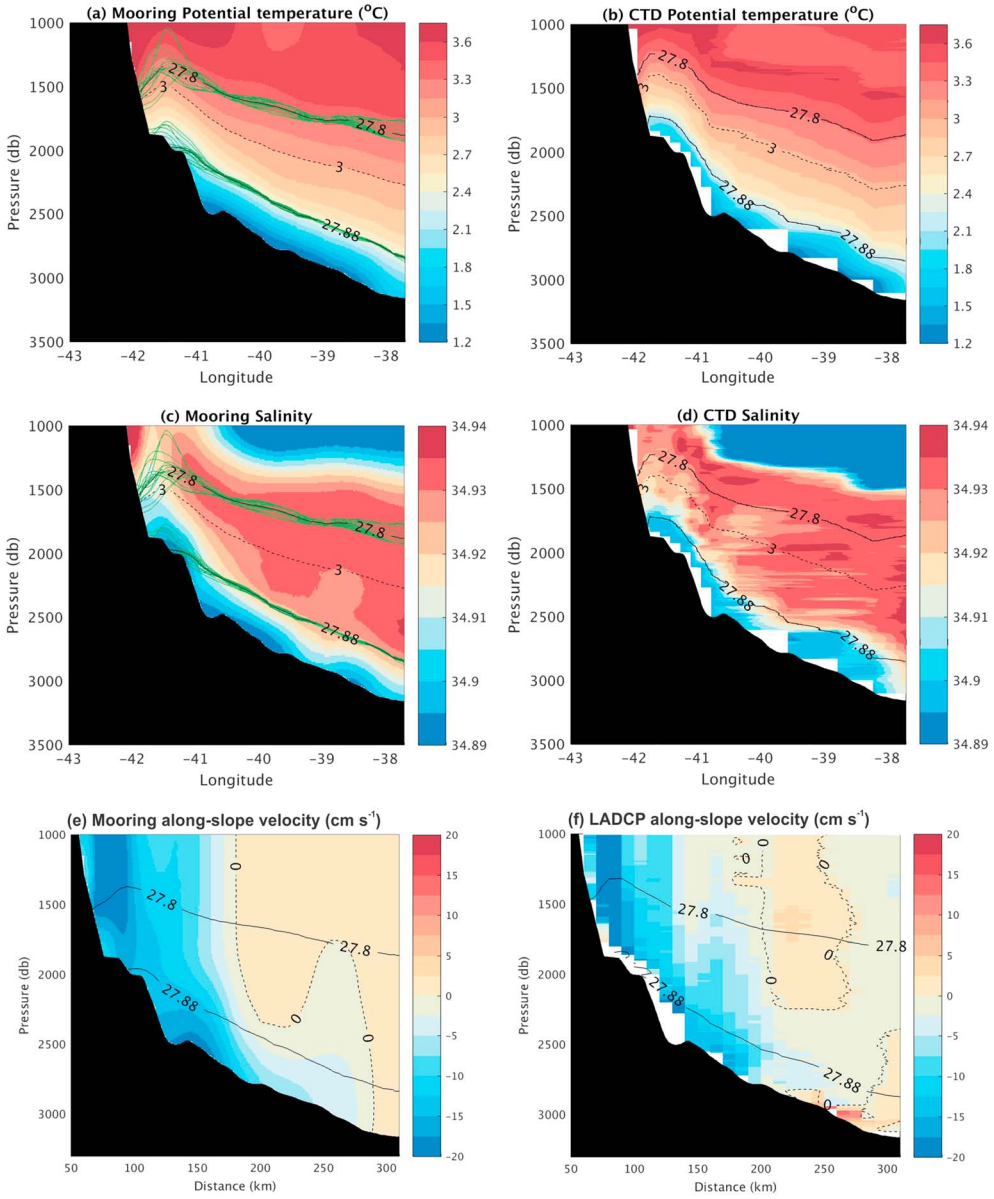

Figure 7. Potential temperature and salinity (a and c) from the mooring array (averaged between 17 and 25 July 2015) compared to the CTD transect completed on cruise PE400 between 17 and 25 July 2015 (b and d). Green isopycnals in (a) and (c) represent the depths of the 27.8- and 27.88-kg/m^3 potential density surfaces from the mooring array every 12 hr during the time of the CTD transect. (e) Deployment mean along-slope velocity (cm/s) from the interpolated mooring data. (f) Average along-slope velocity (cm/s) field from six LADCP sections (September 2005, September 2008, June 2014, August 2014, July 2015, and August 2016). Note the different *x*-axis units in (e) and (f). CTD = conductivity-temperature-depth; LADCP = lowered acoustic Doppler current profiler.

27.88-kg/m^3 isopycnals during this 9-day period, we also plot each 12-hourly snapshot of these bounding density surfaces that the mooring array resolves. This demonstrates that the depth at which both the 27.8- and 27.88-kg/m^3 isopycnals intersect the slope at depths less than 2,000 m varies by several hundred meters on daily time scales.

The deployment-mean along-slope velocity from the mooring array compares well to the average velocity field calculated from the six LADCP sections (Figures 7e and 7f). The core of the DWBC is centered approximately 150 km along the array in a water depth of 2,500 m and has average velocities of 15–20 cm/s. The strength of the current weakens with height above the bottom and distance downslope. The EGIC with

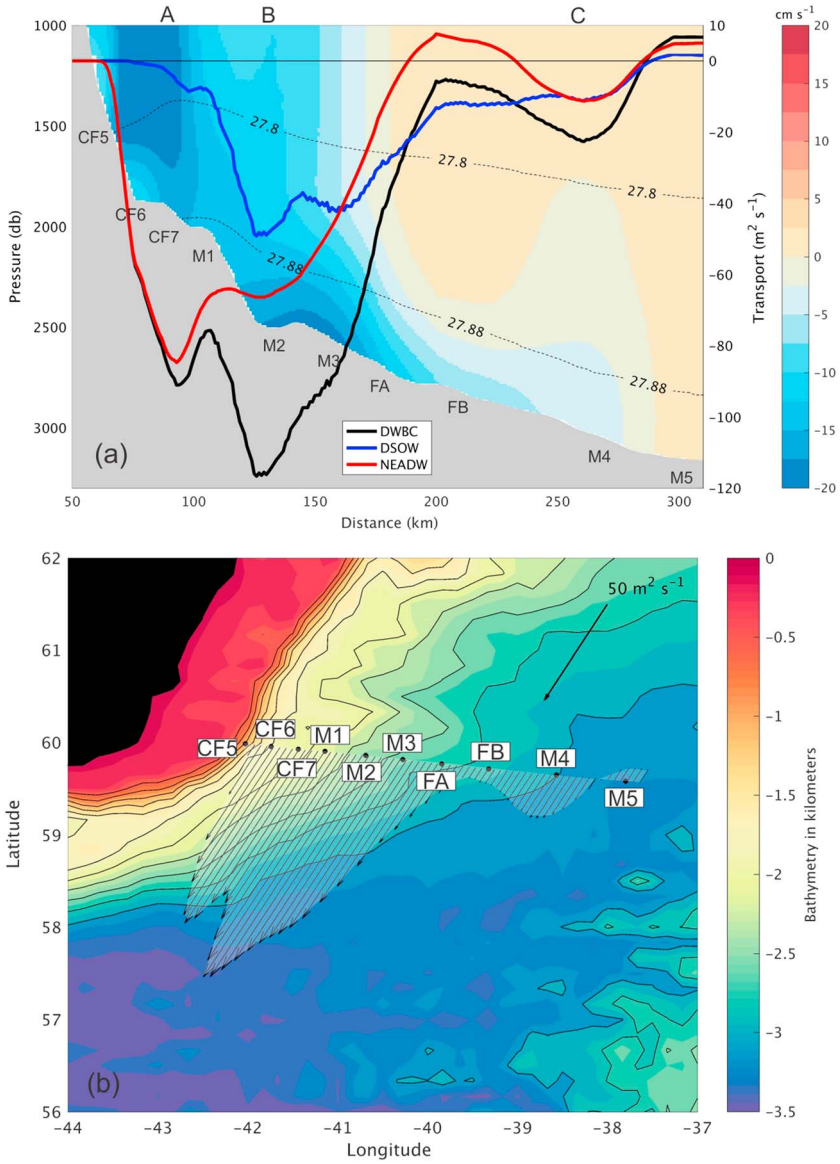

Figure 8. (a) Deployment-mean depth integrated along-slope transport (m^2/s) within the DWBC (black) that crosses the mooring array. Transport associated with the DSOW and NEADW are in blue and red, respectively. Shading is the deployment-mean along-slope velocity (cm/s). (b) Deployment-mean depth integrated along-slope DWBC transport represented as vectors. A–C refer to the spectra plotted in Figure 10. DSOW = Denmark Strait Overflow Water; DWBC = Deep Western Boundary Current; NEADW = North East Atlantic Deep Water.

velocities >20 cm/s is resolved further up the slope in depths <2,000 m. Both the LADCP measurements and the mooring array resolve a similar region of weak positive velocity running through the center of the array.

5. DWBC Transport and Variability

5.1. Deployment-Mean Transport and Structure

The depth integrated deployment-mean along-slope transport within the DWBC (σ_θ > 27.8 kg/m^3) that crosses the mooring array is shown in Figure 8. Maximum transport of the overflow waters occurs at 125 km in a water depth of 2,500 m (marked B). This coincides with the location of the DWBC velocity core. A second transport maximum is located further upslope in 2,000-m water depth at the base of the deep reaching EGIC (marked A). A local transport minimum is located between 200 and 225 km along the

Table 2
Total Transport, Standard Deviation, Standard Error, Decorrelation Time Scales, 95% Boots-Strapped Confidence Interval, and Peak-to-Peak Amplitude for Each Transport Time Series

Water mass	Total transport (Sv)	Standard deviation of total transport (Sv)	Standard error (ε)	Decorrelation time scale (days)	95% bootstrapped confidence interval (lower, upper Sv)	Peak-to-peak amplitude (Sv)
DWBC	−10.8	4.9	0.8	18	(−10.50, −11.02)	31.6
DSOW	−4.1	1.4	0.2	13	(−4.05, −4.20)	9.6
NEADW	−6.5	3.7	0.6	19	(−6.33, −6.72)	24.1

Note. Bootstrapped confidence intervals were obtained based on 10,000 random samples (with replacement). DSOW = Denmark Strait Overflow Water; DWBC = Deep Western Boundary Current; NEADW = North East Atlantic Deep Water.

array in around 2,800 m of water (between moorings FA and FB). There is a further weak maximum between 225 and 275 km in water depths of around 3,000 m (marked C). This coincides with negative deployment-mean velocities that extend from the seafloor up to the 27.8-kg/m^3 isopycnal, on the eastern limit of the deep boundary current. It is worth noting that Bacon and Saunders (2010) identify two separate transport maxima. Their "transport" core, associated with maximum current speeds, is here more clearly subdivided into the EGIC contribution (A) and the transport associated with the deep velocity maximum (B). The magnitude and depth of the deeper (2,900–3,000 m) "property" core described by Bacon and Saunders (2010) matches our offshore transport peak (C).

At mooring M5 there is a weak net poleward transport. The transition from net negative to net poleward transport between moorings M4 and M5 demonstrates that the mooring array extended far enough into the Irminger Basin to capture the whole boundary current.

Transport within the DWBC is divided into the contribution from the densest water mass originating from the Denmark Strait Overflow (DSOW) and from the lighter NEADW (Figure 8a). Maximum transport of DSOW is colocated with the deep velocity core and reduces steadily eastward toward the central basin. The maximum transport of NEADW occurs in around 2,000-m water depth, approximately 50 km west of the main DWBC transport core. Between 189 and 232 km there is a net positive (poleward) transport of NEADW associated with the positive deployment-mean velocities between the 27.8- and 27.88-kg/m^3 isopycnals.

To obtain the total transport we integrate along the mooring line between CF5 and M5, a distance of 241 km. The means, standard deviations, 95% bootstrapped confidence intervals, and peak-to-peak amplitudes are summarized in Table 2. The total transport of the DWBC ($\sigma_\theta > 27.8$ kg/m^3) was -10.8 ± 4.9 Sv (mean $\pm$ 1 std). For DSOW ($\sigma_\theta > 27.88$ kg/m^3) the transport was -4.1 ± 1.4 Sv. Transport within the NEADW density class (27.8–27.88 kg/m^3) was -6.5 ± 3.7 Sv.

Following Bacon and Saunders (2010), we define the standard error (ε) of each estimate using the decorrelation time scale of the transport time series (τ), the record length ($T = 659$ days) and the variance (σ^2) according to $\varepsilon^2 = \sigma^2/(T/\tau)$. The decorrelation time scale is obtained from the zero crossing of the lagged autocorrelation function (Table 2).

5.2. Transport Time Series and Spectra

The transport time series are show in Figure 9. There is a considerable range in transport about the deployment-mean values. Transport variability of the DWBC is characterized by a standard deviation of 4.9 Sv with a peak-to-peak amplitude of 31.6 Sv. Maximum equatorward along-slope transport of −27.6 Sv occurred on 17 October 2014. Less than 1 month earlier, on 28 September 2014 a positive, poleward transport of 4.0 Sv was observed (Figure 9a). Over the measurement period, a net positive DWBC transport occurred on four occasions, all coinciding with positive NEADW transports (Figure 9c). Transport of DSOW was more reliably southward and reached a maximum of −9.1 Sv (Figure 9b). Only on 16 April 2016 did a net northward DSOW transport of 0.6 Sv occur. There is no significant linear temporal trend over the 1.8 years of observations. Variability in volume transport is a function of fluctuations in layer thickness combined with changes in velocity. This is explored in more detail in section 5.3.

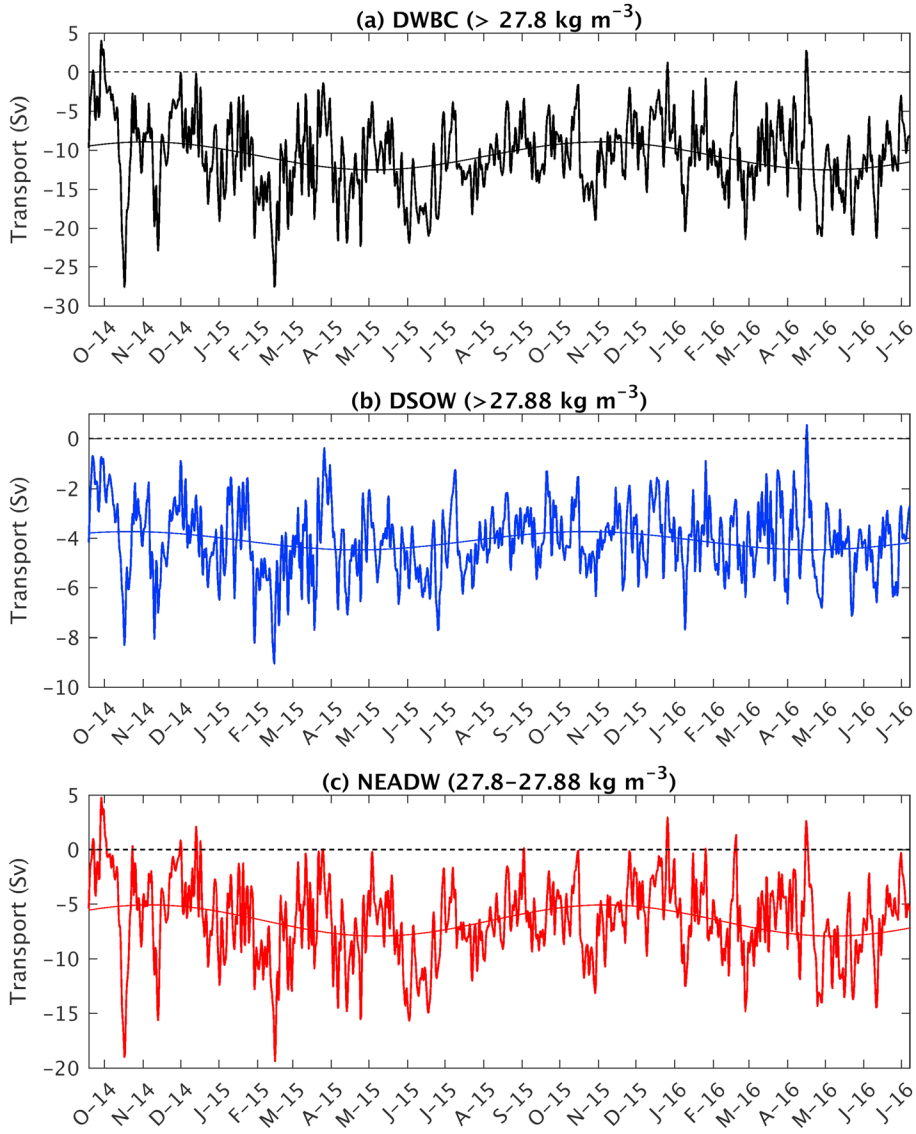

Figure 9. Time series of transport at 12-hourly resolution within (a) the DWBC (Deep Western Boundary Current), (b) DSOW (Denmark Strait Overflow Water), and (c) NEADW (North East Atlantic Deep Water). Thin lines are a harmonically fitted 365-day annual cycle.

An annual cycle has been fitted to each transport time series (Figure 9). Transport is weakest during the winter (October–December) and strongest during the summer (April–June). The DSOW transport leads that of the DWBC as a whole by approximately half a month. The DWBC transport has a seasonal peak-to-trough range of 3.6 Sv (amplitude of 1.8 Sv). The seasonal cycle explains 7%, 8%, and 4% of the variance (p values $\ll$ 0.01) in DWBC, NEADW, and DSOW transports, respectively. These are small but significant contributions.

The power spectral density, presented in its variance preserving form, of each transport time series is shown in Figures 10a and 10b. The spectra were derived following Welch's periodogram method using 220-day segments (with a 50% overlap) and a Hanning window. The 80% confidence intervals are shown. Frequencies where the lower confidence bound exceeds the upper confidence bound for surrounding power spectral density estimates indicate significant oscillations in the time series.

DWBC volume transport has a broad, high-amplitude variance peak between 35- and 65-day periods (Figure 10a). There is also an increase in energy at submonthly time scales, between 3 and 22 days. The amplitude of individual peaks within this frequency range is high and comparable to the amplitude of 35-

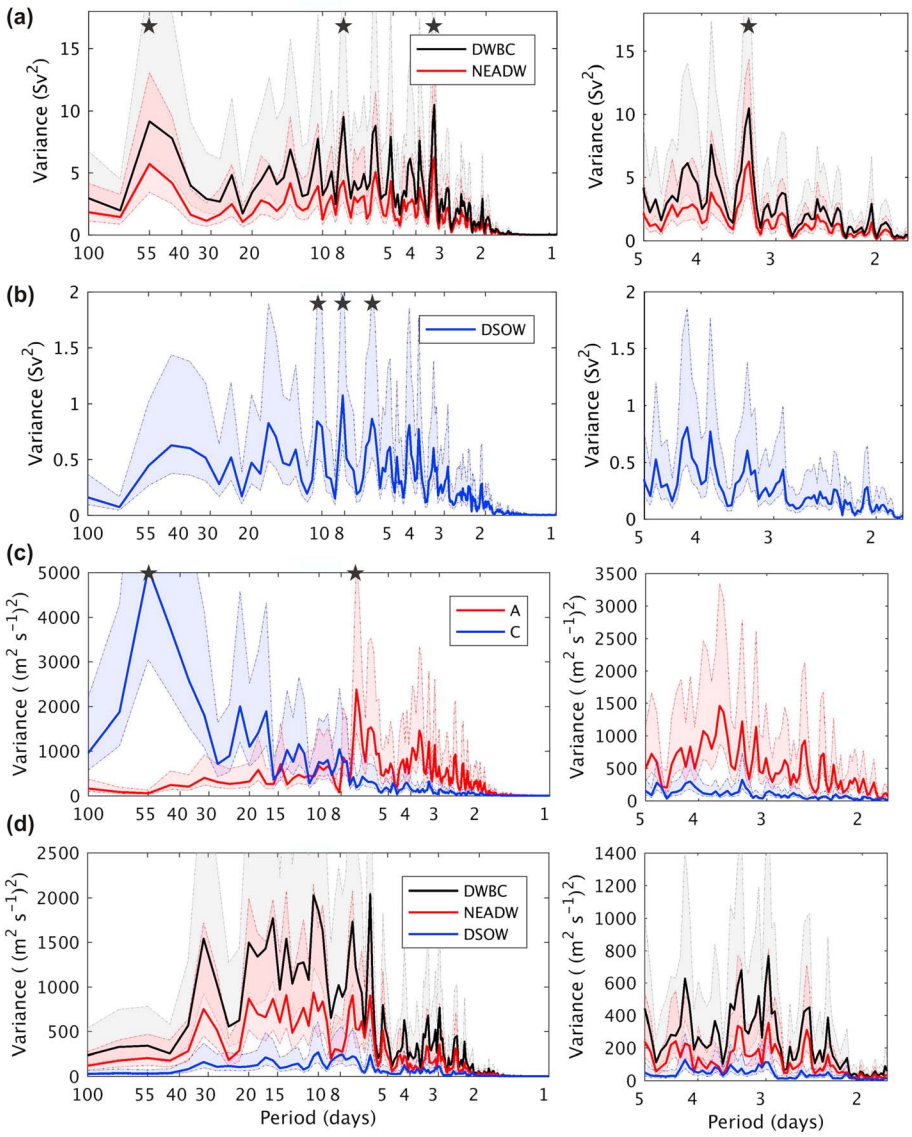

Figure 10. Variance preserving power spectra of (a) the DWBC and NEADW and (b) DSOW transport time series (as in Figure 9). Note that the DSOW spectrum in (b) has a different scale. (c) Depth integrated DWBC transport at the transport maxima marked A and C in Figure 8. (d) Depth integrated transport of DWBC, DSOW, and NEADW at the transport maxima (B). Shading represents the 80% confidence intervals. Stars indicate individual peaks referred to specifically in the text. The right-hand panels are zooms of the power spectra between periods of 1.8 and 5 days. DSOW = Denmark Strait Overflow Water; DWBC = Deep Western Boundary Current; NEADW = North East Atlantic Deep Water.

to 65-day period variability. The three highest-amplitude peaks (in descending order) are at 3.4, 8.2, and 55 days. Transport variability of NEADW is highest at 3.4- and 55-day periods (Figure 10a). In both the DWBC and NEADW time series the peak at 3.4 days is the most significant.

The transport of DSOW has much lower-magnitude variability (Figure 10b). Compared to the DWBC, low-frequency transport variability of DSOW is shifted to slightly shorter periods (30–55 days). Submonthly variability dominates at periods between 3 and 22 days. The greatest variability in DSOW transport is at 8-day periods (significant at the 80% confidence level). Surrounding peaks of a similar magnitude at 10.5 and 6 days are also significant.

Figure 10c shows the power spectra of the depth integrated transport at the transport maxima marked A and C in Figure 8a: (A) under the EGIC where the transport of NEADW dominates, and (C) at the weaker peak

in DWBC transport toward the center of the Irminger Basin. There is a distinct shift from longer periods of transport variability in the deep basin (C) to shorter periods on the upper slope under the EGIC (A). This suggests that the processes contributing to variability in volume transport of the overflow waters, or the frequencies at which they manifest themselves, varies across the slope. On the upper, steeper section of the slope variability is primarily confined to periods between 2.5 and 8 days. The highest amplitude and most significant peak is at 6.8 days (A in Figure 10c). In deep water, toward the eastern limits of the DWBC the amplitude of transport variability increases toward lower frequencies. There is a steady increase in variance between 7 and 25 days. Maximum variability occurs at 55-day periods, significant at the 80% confidence level (C in Figure 10c).

Within the DWBC transport core itself (Figure 10d), the magnitude of variability is moderate. The highest variance is experienced on 5- to 40-day time scales. Although weaker, there is also some transport variability at higher frequencies, matching those that dominate on the upper slope (Figure 10c). Multiple peaks appear within the 2- to 5-day range. Variance at periods longer than 40 days that can be seen in the whole transport time series (Figure 10a), and that are dominant in deeper water (Figure 10c) is absent within the transport core (Figure 10d).

5.3. Eddy Transport Contribution and Layer Thickness

Strong eddy signals in observational data sets from the Irminger Sea are common (Daniault, Lherminier, & Mercier, 2011; Fan et al., 2013; Holliday et al., 2007; Vage et al., 2011). Further south, Peña-Molino et al. (2012) find that Gulf Stream Rings reduce the southward mean transport at 40°N by about 10% (approximately 0.5 Sv within each layer of the DWBC). At the same location, Toole et al. (2017) find that filtering out both the Gulf Stream Rings and Deep Cyclones alters the DWBC transport by 15%. The flow that is blocked by eddies and meanders here must be deflected on a different path. The contribution that the complex and highly energetic eddy field in the Irminger Sea has on DWBC transport variability, however, is unknown.

The passage of an eddy past a mooring is accompanied by a doming (cyclonic) or depression (anticyclonic) of isopycnals. This modifies the layer thickness between two bounding isopycnals. Previous estimates of the transport within the Irminger Sea DWBC have used a mean or synoptic background density field and therefore a fixed layer thickness (Bacon & Saunders, 2010; Clarke, 1984). The spatial and temporal resolution of the CTDs deployed within our mooring array allows us to evaluate the contribution that changes in layer thickness make to the total along-slope transport and its variability. We separate the instantaneous along-slope velocity (v) and layer thickness (h) into their time-mean ($\overline{v}$ and $\overline{h}$) and time-varying (v' and h') or eddy parts. This allows the instantaneous transport (vh) at each location along the array to be written as follows:

$$vh = \overline{v}\,\overline{h} + v'h' + \overline{v}h' + v'\overline{h} \tag{4}$$

The first term on the right-hand side ($\overline{v}\,\overline{h}$) is the transport associated with the mean current acting on the mean layer thickness. The second term ($v'h'$) represents the contribution to transport made by covarying layer thickness and velocity (or the eddy transport). The final two terms describe the variability in transport associated with time-varying layer thickness acting on the mean velocity field ($\overline{v}h'$) and time-varying velocity acting on the mean layer thickness ($v'\overline{h}$). Applying a time average, the final two terms disappear and the time-mean transport can be expressed as follows:

$$\overline{vh} = \overline{v}\,\overline{h} + \overline{v'h'} \tag{5}$$

Note that $\overline{v'h'}$ is able to make a nonzero mean contribution and represents the eddy volume transport. Given that our interpolation scheme (section 4.1) takes into account mooring knock down, we are confident that variability in the inclination of the mooring wire is not generating artificial signals in layer thickness. We also calculate the eddy kinetic energy (EKE) from each current meter where $EKE = 0.5\left(\overline{u'^2} + \overline{v'^2}\right)$ with the over bars representing a time average.

The deployment-mean transport across the entire DWBC is dominated by the contribution associated with the mean velocity and layer thickness ($\overline{v}\,\overline{h}$). The magnitude of the contribution made by the eddy field ($\overline{v'h'}$) is

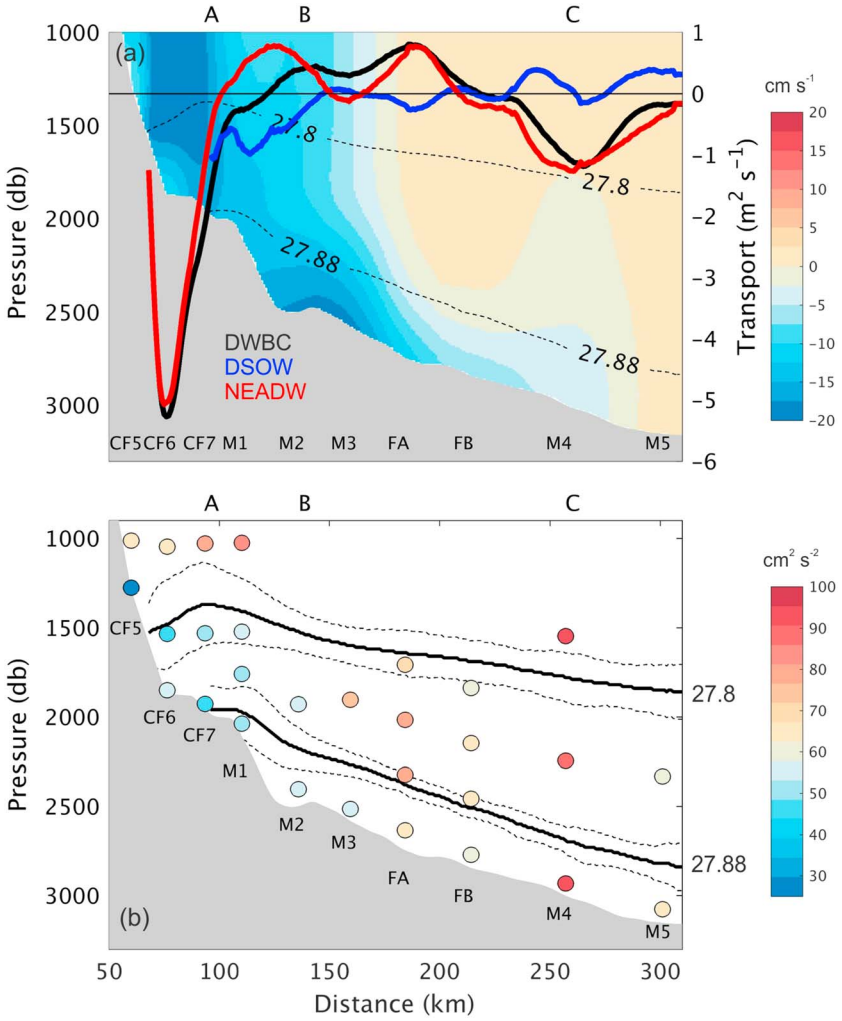

Figure 11. (a) Deployment mean eddy volume transport (m^2/s, right-hand *y* axis) within the DWBC, NEADW, and DSOW. Note that the scale is 20 times smaller than in Figure 8a. Contoured underlay is the deployment mean along-slope velocity field, 27.8- and 27.88-kg/m^3 density contours. (b) Eddy kinetic energy (cm^2/s^2) calculated from each current meter time series. Deployment mean (solid) 27.8- and 27.88-kg/m^3 isopycnal depths plus and minus 2 standard deviations (dashed).

small and typically only a few percent of the deployment mean. However, its contribution varies in both magnitude and sign across the mooring array (Figure 11a).

West of the DWBC velocity core, under the EGIC (A), eddy transport within the DWBC is negative (in the same direction as the EGIC). Of the total −3.1 Sv being transported southward between CF5 and M1, the eddy contribution is just −0.11 Sv (3.5%). Vertical displacement of the 27.8-kg/m^3 isopycnal is greatest at this location (Figure 11b). Interestingly, under the EGIC EKE is higher within the intermediate waters above 27.8 kg/m^3 than in the denser overflow waters below (Figure 11b), indicative of eddy variability that is more baroclinic than elsewhere on the section. Southward eddy transport could arise in one of two ways: (1) southward (negative) v' combined with positive h' (layer thickness increase) or (2) northward (positive) v' and negative h'.

Within the DWBC EKE increases toward the center of the Irminger Basin (Figure 11b). This is reflected in Figure 4 where the near-bed variance ellipses become increasingly isotropic with distance downslope and the velocity histograms become increasingly sinuous and less structured. Eastward of mooring FB a weak negative eddy transport is observed. This coincides with the deeper transport maximum (C) and a band of notably strong EKE that extends from the seafloor into the overlying intermediate water masses

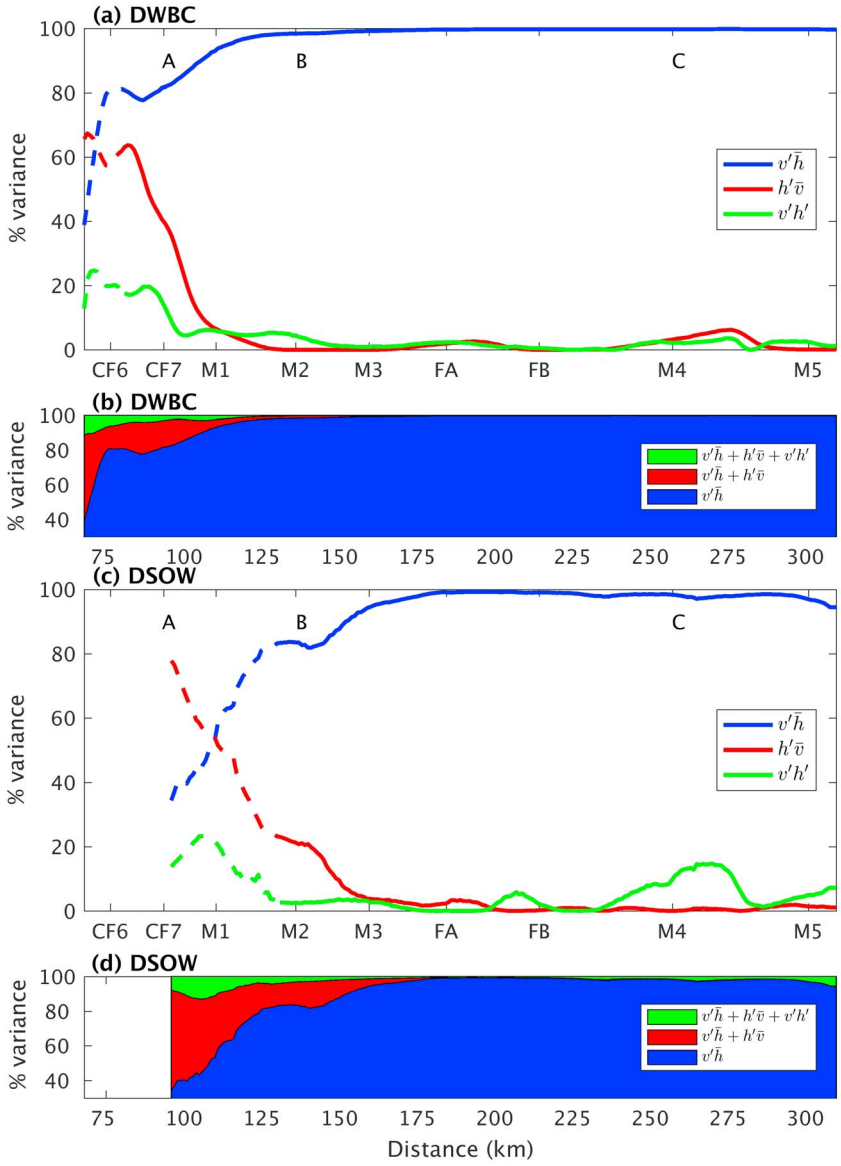

Figure 12. Percentage variance of the instantaneous volume transport (vh) at each location that is explained by $v'\overline{h}$, $h'\overline{v}$ and $v'h'$ (individually) in the (a) DWBC (Deep Western Boundary Current) and (c) DSOW (Denmark Strait Overflow Water). Note that these need not sum to 100%. These plots transition from a dashed to a solid line at the location where the DWBC was always observed within our 1.8-year time series. (b and d) The percentage variance of the instantaneous transport that is explained by the linear combination of terms in the decomposition. A, B, and C mark the locations of the transport maxima (from Figure 8).

(Figure 11b). Between M2 and FB, the covariance between layer thickness and velocity drives a weak, positive (0.04 Sv) volume transport, in opposition to the main southward flow of the DWBC.

Eddy transport within the dense DSOW is also weak. Westward of mooring FB it makes a complementary contribution to the total southward transport. In deeper water to the east there is a weak positive (northward) eddy component. At mooring M5 this is significant. Here, a total of 1.8 m^2/s is transported north, 17% of which (0.3 m^2/s) can be attributed to the eddy term.

Although $v'\overline{h}$ and $\overline{v}h'$ (equation (4)) make zero contribution to the time-mean transport ($\overline{vh}$), decomposing the instantaneous transport time series in this way allows us to assess what the main driver of transport variability is as follows: velocity variability, layer thickness variability, or their covariance. Figures 12a and 12c show the percentage of the instantaneous (vh) DWBC and DSOW transport variance that is individually

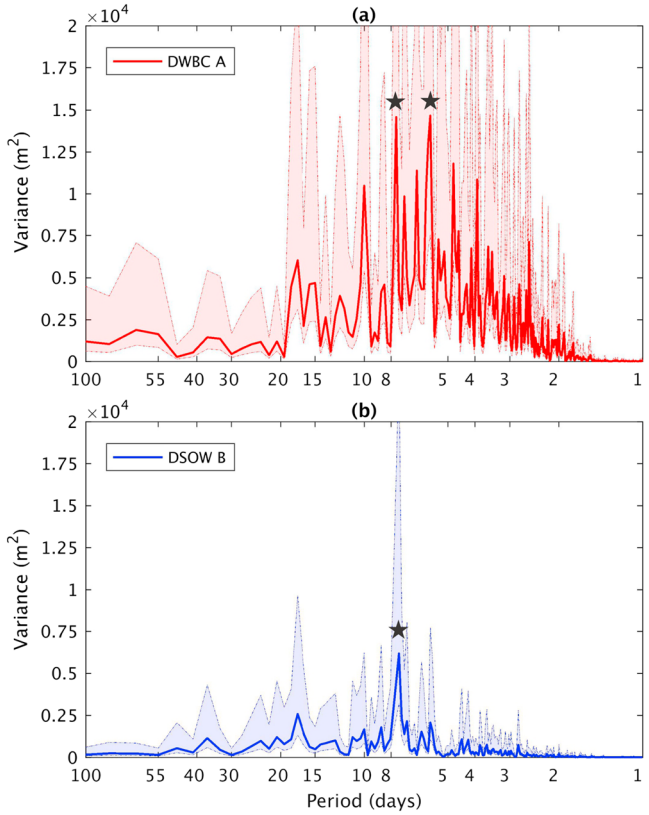

Figure 13. Variance preserving power spectra of (a) DWBC layer thickness at A and (b) DSOW layer thickness at B. Shading represents the 80% confidence interval. Stars mark peaks referred to specifically in the text. DWBC = Deep Western Boundary Current; DSOW = Denmark Strait Overflow Water.

explained by $v'\overline{h}$, $h'\overline{v}$, and $v'h'$. Additionally, in recognition that the full transport time series can only be 100% described by linearly combining all of these terms, Figures 12b and 12d show the cumulative increase in explained variance as more terms are added. Two main results stand out: (1) eastward of the transport core (B), in depths >2,500 m almost all of the instantaneous transport variability is accounted for by variations in velocity acting on mean layer thickness; (2) in shallower water, to the west of the transport core, changes in layer thickness become an increasingly important contributor to transport variance.

In deep water (>2,500 m) over the more gently sloping bathymetry almost all (up to 99%) of the instantaneous variability in DWBC and DSOW transport (vh) can be explained by variations in velocity acting on the mean layer thickness ($v'\overline{h}$, blue lines in Figures 12a and 12c). Within the local transport maximum toward the center of the Irminger Basin (C) 15% of the DSOW transport variability can be explained by $v'h'$, the eddy term (Figure 12c), although there is only a 1.5% contribution to the time-mean transport at this location.

West of the transport core (B), toward the steep continental slope, variability in the layer thickness (h') makes an increasingly important contribution to transport variability. Under the EGIC (A), $h'\overline{v}$ on its own explains up to 60% of the DWBC transport variance (red line in Figure 12a). The eddy term ($v'h'$), again taken in isolation, accounts for up to 20% of the variability of vh at A (green line in Figure 12a). Therefore, west of the transport core, both $h'\overline{v}$ and $v'h'$ are needed to fully resolve the full spectrum of DWBC transport variability (Figure 12b). These findings are supported by a more detailed analysis of the layer thickness. Under the EGIC transport core (A) the deployment-mean layer thickness of water denser than 27.8 kg/m^3 was 560 m, with a standard deviation of 117 m. The highest variance occurs on submonthly time scales, primarily between 3 and 10 days (Figure 13a). The two highest peaks are at 5.7 and 7.6 days, well aligned with the periods of highest transport variance at this location (red line in Figure 10c).

Under the main transport core (B), $h'\overline{v}$ explains 20% of the variability in DSOW transport (red line in Figure 12c). The layer thickness of DSOW water at this location has much weaker variance than changes in thickness of the DWBC under the EGIC (compare Figures 13a and 13b). However, it has a narrower and more significant peak at 7.4 days (blue line in Figure 13b), a feature that is not observed for the lighter 27.8-kg/m^3 isopycnal (not shown). The attribution of potential drivers to the wide range in transport and layer thickness variance will be discussed in section 6.1.

6. Discussion

Our results describe the magnitude, structure, and variability of the DWBC at 60°N in the Irminger Sea between 2014 and 2016, measured for the first time including a time-varying density field. Here, we draw upon previous literature to discuss the potential sources of this variability and consider whether we can reasonably draw on previous transport estimates to infer any long-term (decadal) trend.

6.1. Drivers of Transport Variability

DWBC transport variability in the Irminger Sea is large across a wide range of time scales, from days to months (Figures 10a and 10b). We observe a shift from high- to low-frequency transport variance with increasing depth (Figure 10c), suggesting that the leading order processes driving variability are zonally variable. We have also shown that much of the variance on the western side of the basin is associated with perturbations in the depth of isopycnals bounding the water masses within the DWBC (Figure 12). There are

many processes that might contribute to this variability including topographic waves, propagation of anomalies created upstream, cyclonic and anticyclonic eddies, and recirculation pathways. We will briefly discuss them here and consider whether they are likely to have contributed to the transport variance.

6.1.1. Topographic Rossby Waves

Near-bottom velocity variability characteristic of topographically trapped Rossby waves (TRWs) has been observed all along the path of the DWBC (Fischer et al., 2015; Mertens et al., 2014; Peña-Molino et al., 2012). The period of trapped waves may reasonably range between 7 and 60 days, dependent upon the latitude, the strength of stratification, and the slope of the topography, with a steeper slope leading to higher-frequency waves. TRWs may therefore be responsible for much of the core DWBC transport variance observed here between 5 and 40 days (Figure 10d). At Cape Farewell the slope is first steep and then much gentler, suggesting that higher-frequency TRWs are supported further up the slope, at the western edge of the DWBC. This is consistent with a shift from high- to low-frequency transport variance with increasing distance downslope (Figure 10c). Fischer et al. (2015) report a maximum in velocity variance at a period of 10 days near the core of the DWBC, well aligned with the periods of high variance in volume transport seen here (Figure 10d). They attribute much of this to the passage of TRWs.

6.1.2. Upstream Anomalies and Eddies

Equally, anomalies created upstream of Cape Farewell may impart a signature on the transport of the DWBC. A combination of baroclinic instability and vortex stretching generates near barotropic cyclonic and anticyclonic eddies at the Denmark Strait (Bruce, 1995; Jungclaus et al., 2001; Krauss, 1996; Krauss & Kase, 1998; Spall & Price, 1998). In a modeling study, Krauss and Kase (1998) find that overflow waters trapped between chains of anticyclonic and cyclonic eddies are strongly accelerated by them. Instability on time scales of 2–10 days has been reported for this region (R. R. Dickson & Brown, 1994; Macrander et al., 2005; Smith, 1976). Von Appen et al. (2014) identify cyclonically rotating "boluses" and anticyclonically rotating "pulses" of cold, dense overflow water exiting Denmark Strait on average every 3.4 days and 5.6 days, respectively. As these dense water anomalies sink into deeper water, vortex stretching generates cyclonic eddies that dominate mesoscale variability downstream of the sill. The cyclones may have diameters of 20–100 km and migrate downstream at speeds of 20–30 cm/s, remaining largely trapped within the EGIC, but with a slight downhill component (Bruce, 1995; Krauss, 1996; Krauss & Kase, 1998). At 65°N the separation time between cyclones is between 0 and 8 days (average of 2.1 days; von Appen et al., 2014). Further south at Cape Farewell, cyclonic eddies in water depths of 1,500–2,500 m have been observed (Krauss, 1996). If eddies are generated approximately every 2.1 days it is possible that the 40-hr filter applied to our raw measurements will have dampened their signals.

DWBC transport variability under the EGIC in a water depth of 2,000 m is all at periods between 2 and 8 days (Figure 10c). A large percentage (20–60%) of the instantaneous transport variability at this location can be attributed to displacements of the bounding 27.8-kg/m^3 isopycnal (Figure 12a). Further, variability in DWBC layer thickness under the EGIC is high for periods less than 8 days (Figure 13a). It is therefore likely that cyclonic eddies within the highly energetic and deep reaching EGIC impose high-frequency (<8 days) variability in the transport of the DWBC. The precise mechanics of how this takes place is beyond the scope of the questions being addressed here.

Bacon and Saunders (2010) report maximum transport variability of water colder than 3°C (an isotherm that typically lies ~300 m deeper than the 27.8-kg/m^3 isopycnal) between periods of 10–50 days. They provide little evidence or discussion of mesoscale variability similar to that of Demark Strait overflow cyclones that we see here. Unlike for the transport of water denser than 27.8 kg/m^3 (discussed further in section 6.2) their transport time series for water colder than 3 °C did incorporate a time-varying estimate of the layer thickness. On closer inspection of their power spectra (Figure 10 in Bacon & Saunders, 2010) a peak around 4 days can be seen, although it is much weaker and therefore not discussed. In contrast, we find DWBC transport variance at periods of 3.4, 8.2, and 55 days to be of similar magnitude (Figure 10a). To check that fluctuations in layer thickness are similarly represented in both the 3 °C isotherm and the overlying 27.8-kg/m^3 isopycnal, we calculate their correlation. We find that variability in the depth of the 3 °C isotherm is positively correlated with changes in the depth of the 27.8-kg/m^3 isopycnal at both of the transport maximum. The correlation coefficients at A and B are 0.94 and 0.85, respectively (both significant at the 95% level). This suggests that if significant high-frequency layer thickness variance was present during the Bacon and Saunders (2010) 2005–2006 deployment, their analysis using the 3 °C isotherm could have captured it.

The East Greenland Spill Jet is potentially a further source of variability generated north of Cape Farewell at approximately 65°N (Pickart et al., 2005). It is a bottom intensified flow on the upper slope (around 800 m) composed of dense water that "spills" off the shelf and forms a southward flowing current. There is evidence to show that East Greenland Shelf waters at this latitude are occasionally as dense as the overflow water carried within the DWBC. This results in low salinity anomalies within the 27.8- to 27.88-kg/m^3 density class as far south as Cape Farewell and a transient contribution (from individual events) of up to 25% to the DWBC transport (Falina et al., 2012). Without a coincident record of the hydrography and velocity field across the shelf further north however, we are unable to confidently identify transport anomalies associated with cascading events upstream.

6.1.3. Anticyclonic Eddies in the Central Irminger Basin

Warm, highly energetic, and saline anticyclonic eddies with core diameters in the range 12–20 km and horizontal scales between 20 and 75 km propagate northeast in the upper 1,000 m across the Irminger Basin at speeds of about 0.03 m/s (Fan et al., 2013; Krauss, 1995). They are thought to primarily originate from the EGIC near Cape Farewell (Fan et al., 2013). The salinity records from CTDs mounted above 1,000 m on moorings FA and FB (not used in this study), confirm that high salinity eddies were present in the area during the mooring deployment period.

From an 82-month-long data set collected in the Central Irminger Sea, near to our moorings FA and FB, Fan et al. (2013) identified 44 anticyclonic eddies in the upper 1,000 m. This implies that on average an eddy was observed every 56 days. This is remarkably (or perhaps coincidently) close to the peak in transport variance at 55 days that originates from the weaker, deeper easterly transport maximum of the DWBC (Figures 10a and 10c). Whether the passage of anticyclonic eddies in the upper and intermediate layers have any impact on deeper velocities and density structures in the Irminger Sea is uncertain, although the barotropic nature of the velocity field and coherence of isopyncal depression/uplift over large depth ranges suggests that it is possible. Evidence that circulation features in the Irminger Basin are deep reaching (surface to seafloor) can be found in Holliday et al. (2018).

Interestingly, the 2016 velocity section presented in Holliday et al. (2018) shows a band of southward flow isolated beneath the 27.8-kg/m^3 isopcynal in approximately 3,000 m of water. This coincides with the band of southward velocity in our deployment mean (Figure 6c), the deep water transport maximum (C in Figure 8a), high EKE (Figure 11b) and a deployment-mean southward eddy transport (Figure 11a). We suggest that this may mark the location of persistent deep water eddies in the Irminger Basin.

6.1.4. Recirculations and Retroflections

Recirculations of the middepth cyclonic boundary current are known to drive a return flow that transports water both northward (opposing the boundary current) and eastward into the interior basins of the Labrador and Irminger Seas (Bower & Hunt, 2000; Kase et al., 2001; Lavender et al., 2000). Furthermore, at Cape Farewell, part of the EGIC is retroflected back toward the center of the Irminger Sea (Holliday et al., 2007). Whether or not these recirculations and retroflections play a role in modifying the DWBC transport is unknown.

6.1.5. Seasonality and Entrainment

Lastly, a note on seasonality and entrainment. Transport within the DWBC has a small (amplitude of 1.8 Sv) seasonal cycle (Figure 9). With only 1.8 years of data, however, the robustness of this finding is weak. Seasonality implies a connection to atmospheric processes and in the Irminger Sea deep winter convection is an obvious candidate mechanism (Marshall & Schott, 1999). Deep convection events in both the winter of 2014/2015 and 2015/2016 pushed the depth of the mixed layer down to around 1,600 m at moorings FA and FB during February (de Jong et al., 2018), comparable to the depth of the 27.8-kg/m^3 isopycnal that defines the top of the DWBC. Deep cooling and an increase in LSW density should increase its entrainment into the deep boundary current and thus increase DWBC transport. In our data set there is an increase in transport from January through to middle to late February in both 2015 and 2016, coincident with the deepest and coldest mixed layer reported in de Jong et al. (2018). Admittedly, monthly transport increases of the same magnitude occur at other times of the year. Disentangling transport variability linked to local entrainment within the Irminger Sea, or LSW production and mixing that has occurred either upstream or within the Labrador Sea, and its delayed contribution to transport at 60°N from other processes that can impart variability on monthly time scales is not trivial.

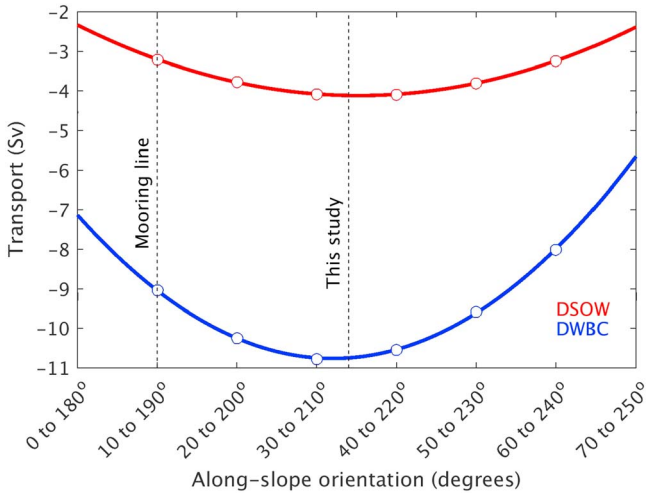

Figure 14. Deep Western Boundary Current (DWBC) and Denmark Strait Overflow Water (DSOW) transport calculated for different definitions of along-slope (open circles). Red and blue lines are quadratic fits. For an along-slope orientation of 30° to 210° negative along-slope velocities head southwest (on a bearing of 210°). Vertical dashed lines mark the transport reported in this study and indicate the definition of along-slope that is normal to the mooring line.

6.2. Sensitivities and Uncertainties of Transport Calculations

Detecting long-term trends by comparing transport estimates derived from independent hydrographic sections made over several decades or from short mooring deployments is challenging. Different types and numbers of instruments are deployed in different locations and at different times, subject to funding sources and project specific interests. Mooring arrays remain in the water for different lengths of time (weeks to years), meaning that they capture differing portions of the full spectra of transport variance. Additionally authors adopt differing analysis techniques, dependent upon the data available to them. All these things introduce different biases into the transport estimates that are made.

Here we quantify how the definition of along-slope velocity, knowledge of the time-varying density field, the length of velocity/density records available, and the limits of integration can bias a transport estimate. In light of these calculations, we assess whether any long-term trend can be confidently inferred from comparison of our estimate with those made by moorings deployed in 1978 and in 2005–2006.

6.2.1. Sensitivity and Biases

We looked carefully at the deployment-mean near-bed velocities and the variance ellipses to determine our definition of along slope. We identified the location of the DWBC velocity core and found the deployment-mean current direction within it to be 214°. Based on this analysis, east-west and north-south velocities were rotated 34° clockwise. Figures 3 and 4, however, demonstrate that the current direction and ellipse orientations vary significantly between the upper and lower reaches of the DWBC, partly in response to changes in the water depth and bathymetric gradient. The mooring array was oriented perpendicular to the isobaths on the upper slope (500–1,000 m) that run between 10° and 190°. Here the lower reaches of the EGIC are strongly topographically constrained. In order to quantify the bias that the definition of along slope makes we calculated the transport for a range of possible orientations, from 10–190° to 60–240°. In each case, we are careful to report only the transport that crosses the mooring line. There are two main points. First, our along-slope definition of 34–214° is one that maximizes the transport (Figure 14). Second, for the DWBC there is a 2-Sv difference between 10–190° and 30–210°. This represents 40% of the transport time series standard deviation. For DSOW transport there is a 1 Sv difference (70% of the standard deviation).

Previous DWBC transport estimates have been made without full knowledge of the time-varying density field (Bacon & Saunders, 2010; Clarke, 1984). The passage of eddies or the propagation of internal waves are examples of how isopycnals may be displaced by tens to hundreds of meters on relatively short (hours to days) time scales. If a single snapshot of the density field, obtained perhaps from a ship-based hydrographic section is used to represent the mean during a current meter deployment, what impact might this have on the final transport estimate? Figure 11b shows the 1.8-year deployment-mean depths of the 27.8- and the 27.88-kg/m^3 isopycnals plus and minus 2 standard deviations. The depth of the 27.8-kg/m^3 isopycnal may quite reasonably vary by 200–400 m. The denser 27.88 kg/m^3 bound by slightly less, 100–300 m. We recalculate transports using isopycnal depths that are 1, 2, and 3 standard deviations above (shallower than) and below (deeper than) the deployment mean (Table A5). For synoptic density sections at times when the 27.8-kg/m^3 isopycnal is 1 std shallower (deeper) than its long-term mean then the transport estimate may be biased 0.9 Sv too high (low). In the extreme 3 std case, then a 3 Sv bias is possible. Calculation of the DWBC transport using the 1.8-year deployment-mean 27.8-kg/m^3 density results in the same estimate of total transport, −10.8 Sv. However, some of the time series variability at higher frequencies is lost. At periods less than 8 days, transport variability is reduced at all the main peaks. Most notably, the magnitude of variance at 6 days decreases from 8.5 to 5.0 Sv^2. This reinforces the idea that higher-frequency variance of DWBC transport has not been fully captured in previous studies.

Uncertainty in the transport estimates is further introduced by recirculations and eddies that make defining the true lateral extent of the boundary current a little subjective. For the densest water (>27.88 kg/m^3) the

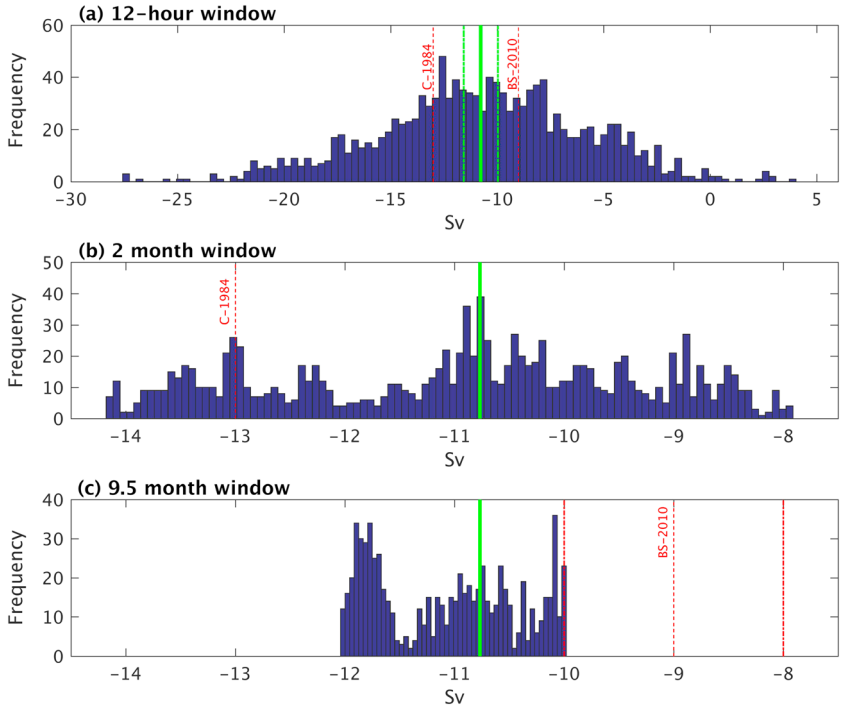

Figure 15. (a) Histograms of individual 12-hr Deep Western Boundary Current transport estimates. Solid vertical green line marks the deployment-mean transport of −10.8 Sv reported here. The dashed green lines either side are 1ε ($\varepsilon = 0.8$). Dashed red lines mark the total transports reported by Bacon & Saunders (2010; BS-2010) and Clark (1984; C-1984). (b and c) Histograms of all the possible transport estimates that could be made within 2- and 9.5-month windows from our data set. Dash-dotted red lines in (c) are 1ε either side of the BS-2010 transport ($\varepsilon = 1$).

deployment-mean velocity and volume transport remains southward right up to the eastern, deep water edge of the DWBC between M4 and M5 (3,126-m water depth; Figure 8a). Within the NEADW layer (27.8–27.88 kg/m^3), however, there are well defined opposing positive and negative bands of mean along-slope velocity within the eastern tail of the boundary current that drive northward and southward transport respectively within that layer (Figure 8a). How far into the basin therefore should we integrate and what impact does this have on the total transport?

If we assume that dynamics within the water column east of 200 km (the location of the DWBC transport minimum in Figure 8a) are primarily dominated by processes other than the boundary current and exclude it from our calculations then we arrive at a total DWBC transport of −9.7 Sv. The 1.1-Sv reduction is accounted for almost entirely (0.8 Sv) by the weaker DSOW contribution. Transport within the NEADW layer remains almost unchanged, reinforcing the idea of a recirculation like feature that makes zero net contribution to the total southward movement of the overflow waters. East of the main velocity core therefore, the majority (>70%) of equatorward transport is within the DSOW layer.

6.2.2. Long-Term Trends

The two most commonly reported estimates of total DWBC transport at this location are from Clarke (1984) and Bacon and Saunders (2010). With 2 months of data Clarke (1984) estimates a transport of −13 Sv. Bacon and Saunders (2010), having a 9.5-month record, arrive at a value of −9 Sv (standard error $\varepsilon = 1$ Sv). Assuming Gaussian statistics, they argue that the 5-Sv reduction in transport between 1978 and 2005–2006 was significant. We can use the same approach here to assess whether the apparent 1.8-Sv increase in transport (from −9 Sv in 2005–2006 to our −10.8 Sv) is likely and what the probability of these values being biased too low or high is.

The probability that our −10.8 Sv is 2.25ε ($\varepsilon = 0.8$) too high and that it should have been −9 Sv or less is 1.2%. Conversely, the probability that the Bacon and Saunders (2010) estimate of −9 Sv should have been −10.8 Sv or more (1.8ε below the true mean) is 3.6%. Based on this alone, it would be reasonable to conclude that there was more than likely a strengthening of DWBC transport between 2005–2006 and 2014–2016. Furthermore,

a 1.8-Sv increase in 10 years, when considered against the decadal scale baroclinic transport variance reported by Bacon (1998), Sarafanov et al. (2009), and Vage et al. (2011), is believable.

However, given that we find transport variance on both seasonal, monthly (spectral peak at 55 days) and daily (peaks at 3–22 days) time scales, it is reasonable to ask whether the timing of the Clarke (1984) and Bacon and Saunders (2010) observations introduced any bias into their final transport estimates (that may not be accounted for in ε). We address this question by subsampling our 1.8-year time series with 2- and 9.5-month windows. We calculate a transport value within each of these windows and plot the results in histogram form (Figure 15). All possible windows are sampled, but there is no repetition. Between 18 September 2014 and 8 July 2016, depending on the time of deployment, a 2-month-long data set would have provided transport estimates anywhere between −8 and −14 Sv (Figure 15b). Based on this alone, the –13 Sv reported by Clarke (1984) seems reasonable. Similarly, 9.5-month-long deployments within this time frame would have yielded transports between −10 and −12 Sv (Figure 15c). It is notable that the Bacon and Saunders (2010) estimate of −9 Sv does not fall within this range. It is 1 Sv weaker than our lowest 9.5-month subsample. Is this additional support for an increase in transport between 2006–2005 and 2014–206, or can this difference (and the 1.8 Sv over the whole deployment period) be reconciled by the assumptions made during the analysis and the limitations of the data available in 2005–2006?

First, the probability that the Bacon and Saunders (2010) estimate should have been −10 Sv or greater, the minimum transport we calculate within each of our 9.5-month windows, is 15.9 %, so not unlikely. This weakens the support for a long-term transport increase.

As demonstrated in Figure 14, the definition of along slope can make a considerable difference to the magnitude of the total transport. Bacon and Saunders (2010) define along slope to have components in the directions 32° and 122°, just 2° different to the coordinate system used here. Based on Figure 14, this would account for just 0.02 Sv and on first impression does not appear to reconcile the missing 1–1.8 Sv. If however, like Bacon and Saunders (2010) and many other authors, we had chosen to define along slope as being perpendicular to our mooring line (with positive and negative components in the directions 10° and 190° respectively), we would have arrived at a total transport estimate of −9 Sv (Figure 14). This would have led to the conclusion of no long-term trend since 2005–2006. It is also worth noting that we report the component of along-slope transport that is normal to our mooring array. Prior to this adjustment our −10.8 Sv was −11.8 Sv (1 Sv more), which is perhaps more directly comparable to the transport that would have crossed the 2005–2006 Bacon and Saunders (2010) line slightly further south. From this perspective, the argument for an increase in long-term transport strengthens.

Other methodological differences worth considering are the integration limits and the lack of dense water layer thickness measurements available to Bacon and Saunders (2010). To obtain the entire transport in the DWBC, Bacon and Saunders (2010) integrate along their mooring line up until the mean depth integrated transport becomes northward (at a depth of 3,073 m). If we apply the same criteria here and integrate to the zero crossing point in depth integrated transport (286 km and 3,126-m depth in Figure 8a), our southward transport estimate is increased by 0.06 Sv. Definition of the eastward DWBC limit cannot therefore account for the reduced 2005–2006 transport. However, in Bacon and Saunders (2010) the mean depth of the 27.8-kg/m^3 density surface was derived from two CTD sections taken on the mooring deployment and recovery cruises. It is possible that the additional 1.8 Sv found here could be explained by the CTD sections in 2005 and 2006 being done at times when the 27.8-kg/m^3 isopycnal was sitting (between 1 and 2 stds) deeper than average in the water column and biasing the transport estimate too low (see Table A5). Given that the two mooring lines were not exactly in the same location, however, it is difficult to confidently make a comparison.

In summary, we are able to weaken the conclusion of a transport increase between 2005–2006 and 2014–2016 significantly, by factoring in the biases introduced by the definition of along slope and a lack of information on the time-varying thickness of the DWBC.

7. Conclusions

The first two years (2014–2016) of data collected from the OSNAP mooring array in the Irminger Sea have been used to examine the structure of the DWBC and to calculate its volume transport. A total of 24

current meters and 5 ADCPs reveal a wide (125 km) zone of equatorward flow extending from the seafloor to 1,000 m. Within the 50-km-wide core of the boundary current, in around 2,500 m of water, current speeds are on average 20 cm/s and decrease with height above the seafloor. Eastward of the velocity core, toward the center of the Irminger Basin, the thickness of the DWBC reduces and net southward flow is primarily restricted to the deepest, densest layers.

We calculate a 1.8-year mean transport of -10.8 ± 4.9 Sv (mean $\pm$ 1 std) for water denser than 27.8 kg/m^3. Of this total, we find -4.1 ± 1.4 Sv within the DSOW layer ($\sigma_\theta > 27.88$ kg/m^3) and -6.5 ± 3.7 Sv within the NEADW layer (27.8–27.88 kg/m^3). There is evidence of a recirculation feature within the NEADW layer, east of the main DWBC velocity core that makes very little contribution to the time-mean transport.

Total transport variability ranges from days to months (2–65 days). Within the core of the DWBC variability occurs on 5- to 40-day time scales. There is a distinct shift from high- to low-frequency variance with distance from the East Greenland continental slope. On the western, upper slopes under the EGIC, where the flow is strongly topographically steered, most of the transport variance is between 2 and 8 days. In contrast, the deepest, most eastern limb of the DWBC, where the greatest velocity variance is across, rather than along, isobaths, introduces transport variance at around 55 days.

Although the time-mean eddy volume transport across the array is small, time-varying perturbations in layer thickness under the EGIC make an important (20–60%) contribution to the magnitude and frequency of transport variance at this location. Topographic Rossby waves and cyclonic eddies propagating southward within the western boundary current system are most likely to be responsible for much of the higher-frequency variability observed here. Toward the center of the basin, anticyclonic eddies and recirculations may impose some of the lower-frequency variability, although this is more speculative. A weak seasonal transport signal was observed, but this will be more confidently explored once the next two years (2016–2018) worth of OSNAP data have been analyzed.

The OSNAP Irminger Sea DWBC array was designed to measure the total volume transport of the deep overflow waters that drive the lower limb of the AMOC. The results presented here demonstrate that the design was fit for purpose. The transport core and its dynamics are well resolved by instrumentation separated by distances that are close to or below the horizontal and vertical decorrelation length scales of temperature (r_h = 39–45 km, r_v = 517–600 m), salinity (r_h = 32–36 km, r_v = 295–321 m), and velocity (r_h = 18–24 km, r_v = 1,400 m). The deployment-mean transport becomes positive between moorings M4 and M5, confirming that M5 was located far enough east.

Based on Gaussian statistics, a 1.8-Sv increase in total DWBC transport since 2005–2006 seems probable. However, the potential biases introduced by (a) the definition of along slope (1–2 Sv) and (b) a lack of information on the time-varying thickness of the dense water layers in 2005–2006 (1 Sv) could comfortably account for this increase. We conclude that the 2014–2016 transport calculated here cannot be confidently compared to observations and calculations made in the past to infer any long-term trends.

Appendix A: Data Processing and Interpolation Details

A1. Gap Filling Procedures

A 115-day period of missing data (25 March to 17 July 2015) from the SBE37 at 2,305 m depth on M5 was filled by taking advantage of the close correlation (R^2 of 0.5–0.6, p value $\ll 0.01$) in temperature and salinity fluctuations with instrumentation mounted higher and lower in the water column. The mean temperature (salinity) anomaly time series of instruments 360 m above and below was added to the mean temperature (salinity) recorded over the preceding 228 days. The baseline pressure was calculated by taking an average over a preceding period (where there was no knockdown). The mean pressure anomaly of the instruments above and below was subsequently added to this baseline. A short 32-day gap in salinity between 20 January and 21 February 2015 nominally at 2,200 m on M4 was filled using the same approach.

We take advantage of the barotropic nature of the velocity field to estimate what the faulty ADCP deployed at M4 in 2014 would have recorded. A linear regression between the fourth bin (nominal depth of 2,927 m) of the M4 ADCP deployed between 21 July 2015 and 4 August 2016 and the Nortek current meter 678 m above was performed (using the low pass filtered and 12-hr averaged time series; Figure A1). The linear fit for both

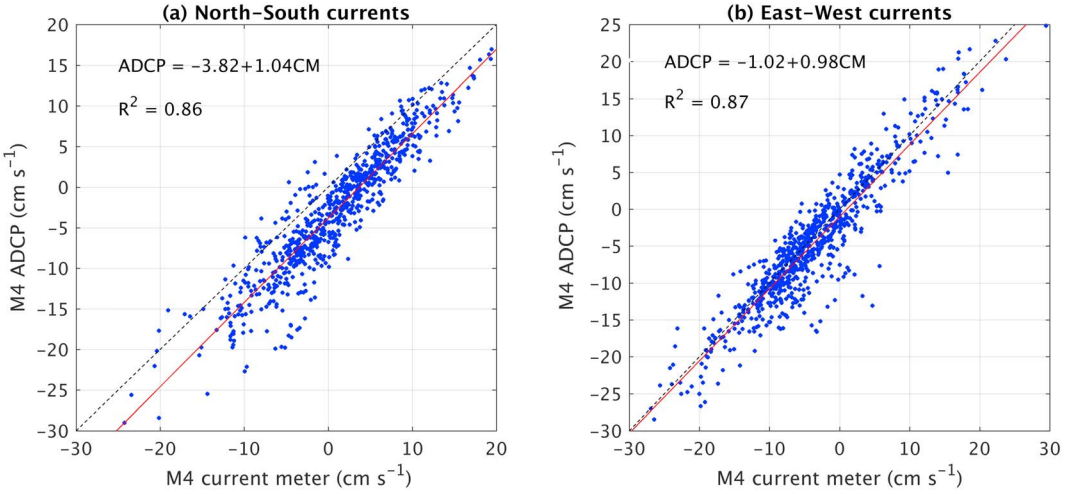

Figure A1. Linear regression between the (a) north-south and (b) east-west velocities recorded by the M4 current meter (average depth of 2,249 m) and the fourth bin of the M4 acoustic Doppler current profiler (ADCP; average depth of 2,927 m) between 21 July and 4 August 2015. P values $\ll 0.01$. Velocities used here have been low-pass filtered and 12 hr averaged. Red lines are the linear fit.

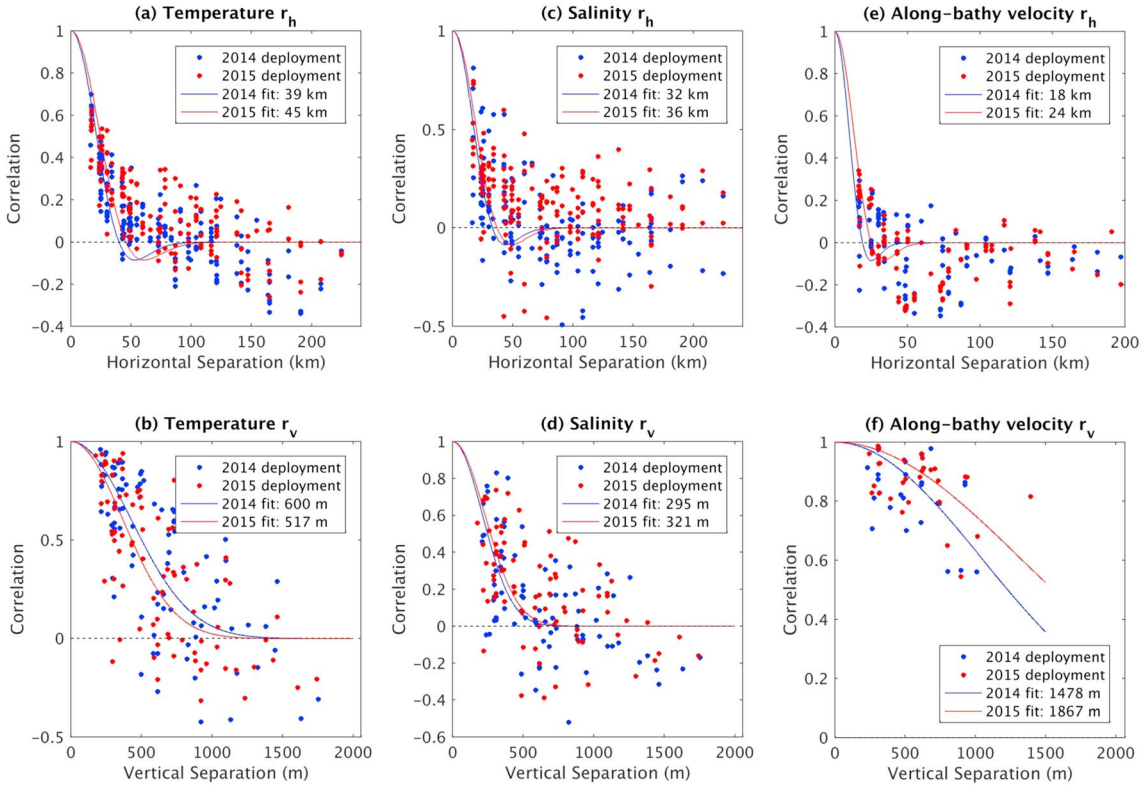

Figure A2. Cross correlations of pairs of temperature (a and b) salinity (c and d) and along-slope velocity (e and f) records in the horizontal (top panels) and vertical (bottom panels), as a function of their separation distance. For the horizontal, only pairs within a spread of 200 m in the vertical are used. Length scales are obtained from the fit to covariance functions (equations (A1) and (A2)). Only having current meters below 1,500 m beyond mooring M1 (and not using any instruments higher than 1,000 m in the water column) means that the fit of the covariance function in the vertical is not well constrained.

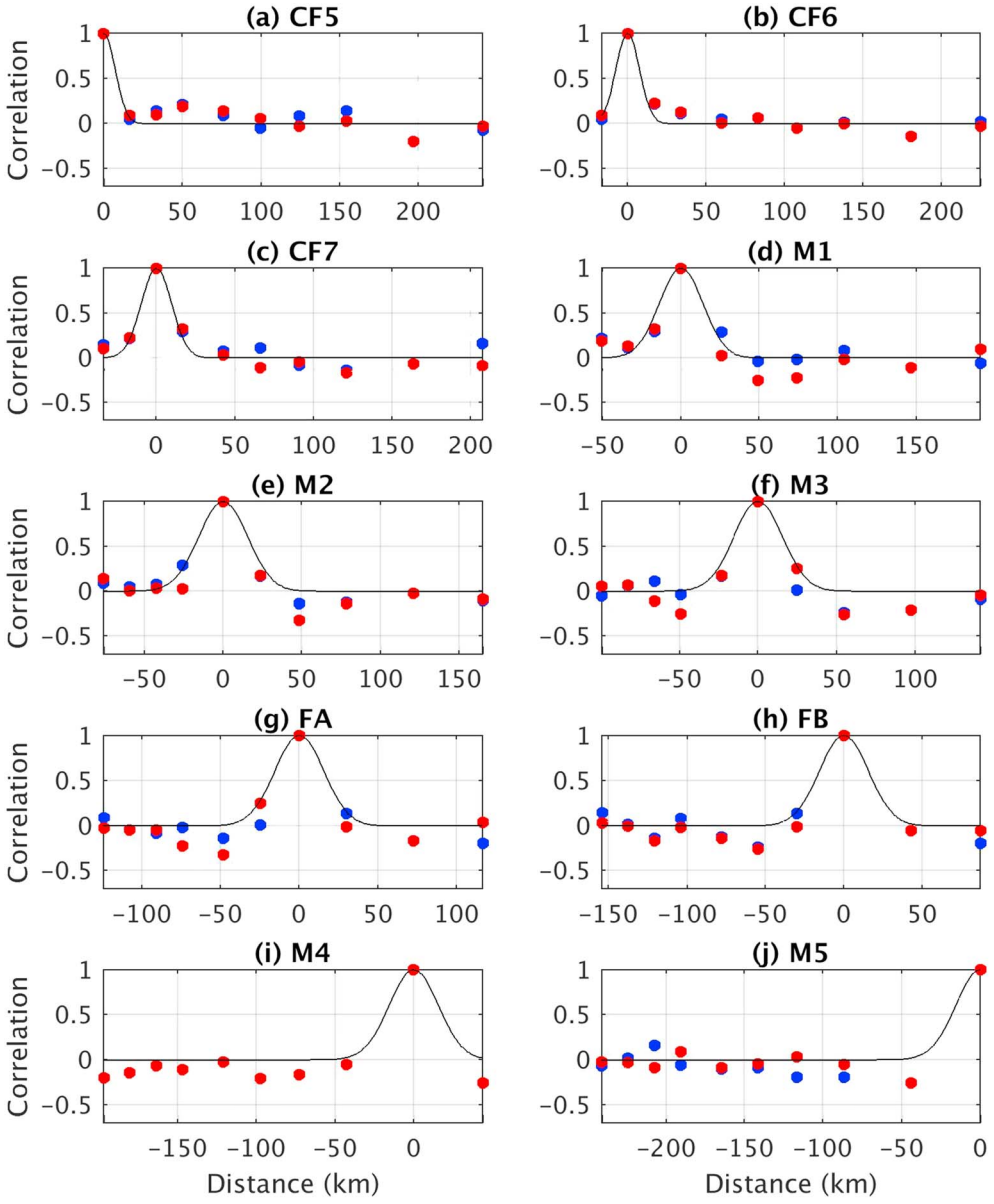

Figure A3. Zero lag correlations of the near bottom along-slope velocity records at each mooring as a function of separation distance: 2014 deployment in blue and 2015 deployment in red. The black curve in each plot represents the horizontal decay in weighting applied during the interpolation at each location (see Table 1). It increases from 10 km at CF5 to 30 km at M5.

the north-south and east-west components of the flow (R^2 of 0.86–0.87, p values $\ll 0.01$) was then used to estimate velocities at 2,932 m depth between 9 August 2014 and 17 July 2015.

A2. Decorrelation Length Scales

We fit covariance functions to the horizontal and vertical correlations (ρ_h and ρ_v) between pairs of (40-hr low-pass filtered and 12 hr averaged) temperature, salinity and velocity records as a function of their separation distance. This is performed separately for the 2014 and 2015 deployments, selecting only the times when all the instrumentation was in the water (301 and 321 days, respectively). Following Beal et al. (2015) we assume the horizontal and vertical covariance functions to have the form

Table A1
Mooring Locations, Water Depths, Deployment and Recovery Times, Distance of Moorings from the 50-m Isobath, and Gaps in Data Streams Resulting From Mooring Servicing

Mooring	Latitude	Longitude	Total water depth (m)	Distance (km) from 50-m isobath	Date of first deployment	Date of final recovery	Gap in data streams resulting from mooring servicing (hours)
CF5	59.9881	−42.0260	1,270	60	14/08/2014	11/08/2016	0
CF6	59.9579	−41.7395	1,852	76	12/08/2014	08/08/2016	0
CF7	59.9264	−41.4377	1,928	94	12/08/2014	08/08/2016	0
M1	59.9041	−41.1401	2,070	110	11/08/2014	30/07/2016	44
M2	59.8593	−40.6888	2,488	136	10/08/2014	30/07/2016	34
M3	59.81	−40.28	2,559	160	09/08/2014	01/08/2016	33
FA	59.7668	−39.8425	2,646	184	12/09/2014	12/08/2017	55
FB	59.7128	−39.3204	2,780	214	17/09/2014	11/08/2017	82
M4	59.65	−38.57	2,985	257	08/08/2014	04/08/2016	80
M5	59.58	−37.80	3,125	301	08/08/2014	05/08/2016	80

Table A2
Conductivity, Temperature, and Depth Instrumentation Used in This Study

Mooring	Instrument type	Target depths (m)	Sampling interval
CF5	SBE37	750, 1,000, and 1,275	15 min
CF6	SBE37	750, 1,000, 1,500, and 1,830	15 min
CF7	SBE37	750, 1,000, 1,500, and 1,900	15 min
M1	SBE37	750, 1,005, 1,250, 1,490, 1,730, and 1,955	60 min
M2	SBE37	1,585, 1,800, 2,020, 2,230, and 2,440	60 min
M3	SBE37	1,325, 1,615, 1,905, 2,195, and 2,480	60 min
FA	SBE37	1,000*, 1,500*, 1,800, 2,100, 2,400, and 2,700	*15 min and 7.5 min
FB	SBE37	1,000*, 1,500*, 1,800, 2,100, 2,400, and 2,700	*15 min and 7.5 min
M4	SBE37	1,520, 1,860, 2,200, 2,540, and 2,875	60 min
M5	SBE37	1,585, 1,945, 2,305, 2,665, and 3,020	60 min

Note. Asterisks for FA and FB indicate instruments recording every 15 minutes (as opposed to 7.5 minutes).

Table A3
Current Meters and ADCPs Used in This Study

Mooring	Instrument type	Target depth (m)	Sampling interval
CF5	Nortek	1,000 and 1,266	30 min
CF6	Nortek	1,000, 1,500, and 1,821	30 min
CF7	Nortek	1,000, 1,500, and 1,891	30 min
M1	Nortek	1,000, 1,485, 1,725, and 1,965	60 min
M1	300-kHz RDI ADCP	1,965	60 min
M2	Nortek	2,015	60 min
M2	300-kHz RDI ADCP	2,450	60 min
M3	Nortek	1,900	60 min
M3	300-kHz RDI ADCP	2,490	60 min
FA	Nortek	1,800, 2,100, 2,400, and 2,700	60 min
FB	Nortek	1,800, 2,100, 2,400, and 2,700	60 min
M4	Nortek	1,515 and 2,195	60 min
M4	300-kHz RDI ADCP	2,880	60 min
M5	Nortek	2,300	60 min
M5	300-kHz RDI ADCP	3,025	60 min

Note. ADCP = acoustic Doppler current profiler.

Table A4
Minimum, Maximum, Mean, and Standard Deviation (std) of the Root-Mean-Square Deviation Between Observed and Interpolated Values of the Temperature, Salinity, and Along-Slope Velocity

Variable	min	max	mean	std
Temperature (°C)	0.004	0.14	0.04	0.03
Salinity	3.8×10^{-4}	8.7×10^{-3}	3×10^{-3}	2×10^{-3}
Along-slope velocity (cm/s)	0.009	3.3	1.4	0.9

Table A5
Volume Transport of DWBC and DSOW Recalculated Using Isopycnal Surfaces That Are 1, 2, and 3 Standard Deviations Above and Below Their Deployment Means

Water mass	Above mean (shallower)	Below mean (deeper)	Bias (Sv)
DWBC (−10.8 Sv for a fixed, deployment-mean 27.8-kg/m^3 isopycnal depth)			
1 std	−11.7 Sv	−9.6 Sv	0.9 Sv
2 std	−12.7 Sv	−8.7 Sv	2.1 Sv
3 std	−13.8 Sv	−7.9 Sv	3 Sv
DSOW (−4.1 Sv for a fixed, deployment-mean 27.88-kg/m^3 isopycnal depth)			
1 std	−4.7 Sv	−3.5 Sv	0.6 Sv
2 std	−5.4 Sv	−2.9 Sv	1.3 Sv
3 std	−6.1 Sv	−2.4 Sv	2 Sv

Note. DSOW = Denmark Strait Overflow Water; DWBC = Deep Western Boundary Current.

$$\rho_h(r) = e^{-\left(r/r_h\right)^2} \cos\left(\frac{\pi r}{2r_h}\right) \quad \text{(A1)}$$

and

$$\rho_v(z) = e^{-\left(z/r_v\right)^2} \quad \text{(A2)}$$

respectively, where r_h and r_v are the decorrelation length scales in the horizontal and vertical, and r and z are the horizontal (km) and vertical (m) separation distances. A nonlinear fitting algorithm (Nelder & Mead, 1965) is used to find r_h and r_v (Figure A2).

A3. Preparation for Optimal Interpolation

A 1,000-m value of temperature and salinity at M2 and M3 was generated by linearly interpolating between the 1,000-m CTDs on M1 and FA. At M4 and M5 temperature and salinity at 1,000 m was set equal to the 1,000-m observation at FB. Hydrographic sections (e.g., Figures 7b and 7d) confirm that LSW occupies intermediate depths across the Irminger Basin. The deployment mean salinity shown in Figure 2b indicates that the 1,000-m CTD on mooring FB was sampling LSW and is the best available estimate of the properties at 1,000 m further out into the basin. Given that, the DWBC at M4 and M5 is always deeper than 1,500 m, this intermediate depth (horizontal) extrapolation serves mainly to force a more realistic vertical gradient in density above 1,500 m at M4 and M5 than would otherwise have been achieved by a vertical interpolation. Linear vertical interpolation was then used to increase the resolution of data points on each mooring to approximately 100-m intervals. This served to reduce both the vertical distance of the search radius and σ_z. The depth of each vertically interpolated value varies at each time step depending on instrument knock down.

The velocity field was extended to 1,000 m at moorings M2, M3, FA, FB, M4, and M5 by simply replicating the velocity from the shallowest instrument. This is justified given the strong barotropic nature of the flow and the short horizontal decorrelation length scale (Figure A2f). Furthermore, at three of these moorings (FA, FB and M4) there were current meters deployed above or very close to the mean depth of the 27.8-kg/m^3 isopycnal, the upper boundary of the DWBC (Figure 11b). This interpolation therefore has minimal impact on the velocities within the DWBC at these locations. At the other moorings, the shallowest current meters were 400 m (M2), 300 m (M3), and 490 m (M5) below the mean 27.8-kg/m^3 isopycnal (Figure 11b), vertical distances that are all significantly less than the 1,478- to 1,867-m decorrelation length scales estimated above (Figure A2f).

Moorings M1 and M2 are separated by a steep rise in the bathymetry. Data points were introduced half way up this slope at 50 and 200 m above the seafloor, calculated using a local along-bottom linear interpolation. This helps reduce discontinuities in the flow within the deep core of the DWBC.

Acknowledgments
This work was supported by the NERC U.K. OSNAP program (NE/K010875/1 and NE/K010700/1) and the U.S. National Science Foundation (Grant OCE-1258823). The U.K. mooring data are available from the British Oceanographic Data Centre (doi:10.5285/6cb6dc0c-7bed-3ca4-e053-6c86abc0b9f0). Data from the U.S. OSNAP East Greenland Current mooring section are available from the repository (doi:10.7924/r4fb50z9b). Data from moorings FA and FB may be downloaded from the Ocean Observatories Initiative data portal (https://oceanobservatories.org). All hydrographic and LADCP data from cruises DY054, D298, D332, and JR302 are available from the British Oceanographic Data Centre. Hydrographic data from KN221 and PE400 are available from the following DOIs (doi.org/10.7924/r4qz26535 and doi.org/10.17882/59302 respectively). The authors wish to thank two anonymous reviewers for their suggestions that have improved this manuscript and all the technical staff, ship's crew, and OSNAP scientists who made the collection of these data sets possible.

References

von Appen, W. J., Pickart, R. S., Brink, K. H., & Haine, T. W. N. (2014). Water column structure and statistics of Denmark Strait Overflow Water cyclones. *Deep-Sea Research Part I-Oceanographic Research Papers*, *84*, 110–126. https://doi.org/10.1016/j.dsr.2013.10.007

Bacon, S. (1997). Circulation and fluxes in the North Atlantic between Greenland and Ireland. *Journal of Physical Oceanography*, *27*(7), 1420–1435. https://doi.org/10.1175/1520-0485(1997)027<1420:cafitn>2.0.co;2

Bacon, S. (1998). Decadal variability in the outflow from the Nordic seas to the deep Atlantic Ocean. *Nature*, *394*(6696), 871–874. https://doi.org/10.1038/29736

Bacon, S., Reverdin, G., Rigor, I. G., & Snaith, H. M. (2002). A freshwater jet on the east Greenland shelf. *Journal of Geophysical Research*, *107*(C7), 3068. https://doi.org/10.1029/2001jc000935

Bacon, S., & Saunders, P. M. (2010). The Deep Western Boundary Current at Cape Farewell: Results from a Moored Current Meter Array. *Journal of Physical Oceanography*, *40*(4), 815–829. https://doi.org/10.1175/2009jpo4091.1

Barnes, S. L. (1964). A technique for maximizing details in numerical weather map analysis. *Journal of Applied Meterology*, *3*(4), 396–409. https://doi.org/10.1175/1520-0450(1964)003<0396:ATFMDI>2.0.CO;2

Barnes, S. L. (1973). Mesoscale objective map analysis using weighted time-series observations. NOAA Tech. Memo. ERL NSSL-62. National Severe Storms Laboratory, Norman, Oklahoma.

Beal, L. M., Elipot, S., Houk, A., & Leber, G. M. (2015). Capturing the transport variability of a western boundary jet: Results from the Agulhas Current Time-Series Experiment (ACT). *Journal of Physical Oceanography*, *45*(5), 1302–1324. https://doi.org/10.1175/jpo-d-14-0119.1

Bersch, M. (1995). On the circulation of the northeastern North-Atlantic. *Deep-Sea Research Part I-Oceanographic Research Papers*, *42*(9), 1583–1607. https://doi.org/10.1016/0967-0637(95)00071-d

Bower, A. S., & Hunt, H. D. (2000). Lagrangian observations of the deep western boundary current in the North Atlantic Ocean. Part I: Large-scale pathways and spreading rates. *Journal of Physical Oceanography*, *30*(5), 764–783. https://doi.org/10.1175/1520-0485(2000)030<0764:lootdw>2.0.co;2

Bower, A. S., Lozier, M. S., Gary, S. F., & Boning, C. W. (2009). Interior pathways of the North Atlantic meridional overturning circulation. *Nature*, *459*(7244), 243–U126. https://doi.org/10.1038/nature07979

Bruce, J. G. (1995). Eddies southwest of the Denmark Strait. *Deep-Sea Research Part I-Oceanographic Research Papers*, *42*(1), 13–29. https://doi.org/10.1016/0967-0637(94)00040-y

Chelton, D. B., DeSzoeke, R. A., Schlax, M. G., El Naggar, K., & Siwertz, N. (1998). Geographical variability of the first baroclinic Rossby radius of deformation. *Journal of Physical Oceanography*, *28*(3), 433–460. https://doi.org/10.1175/1520-0485(1998)028<0433:GVOTFB>2.0.CO;2

Clarke, R. A. (1984). Transport through the Cape Farewell-Flemish Cap section. Rapp. P.-V. Reun.- Cons. Int. Explor. Mer, 185, 120-130.

Danabasoglu, G., Yeager, S. G., Kim, W. M., Behrens, E., Bentsen, M., Bi, D. H., et al. (2016). North Atlantic simulations in Coordinated Ocean-ice Reference Experiments phase II (CORE-II). Part II: Inter-annual to decadal variability. *Ocean Modelling*, *97*, 65–90. https://doi.org/10.1016/j.ocemod.2015.11.007

Daniault, N., Lherminier, P., & Mercier, H. (2011). Circulation and transport at the southeast tip of Greenland. *Journal of Physical Oceanography*, *41*(3), 437–457. https://doi.org/10.1175/2010jpo4428.1

Daniault, N., Mercier, H., & Lherminier, P. (2011). The 1992-2009 transport variability of the East Greenland-Irminger Current at 60 degrees N. *Geophysical Research Letters*, *38*, L07601. https://doi.org/10.1029/2011GL046863

Daniault, N., Mercier, H., Lherminier, P., Sarafanov, A., Falina, A., Zunino, P., et al. (2016). The northern North Atlantic Ocean mean circulation in the early 21st century. *Progress in Oceanography*, *146*, 142–158. https://doi.org/10.1016/j.pocean.2016.06.007

Dickson, B., Dye, S., Jónsson, S., Köhl, A., Macrander, A., Marnela, M., et al. (2008). The overflow flux west of Iceland: Variability, origins and forcing. In R. R. Dickson, J. Meincke, & P. Rhines (Eds.), *Arctic–Subarctic Ocean Fluxes: Defining the Role of the Northern Seas in Climate*, (pp. 443–474). Dordrecht: Springer Netherlands.

Dickson, R. R., & Brown, J. (1994). The production of North-Atlantic Deep Water: Sources, rates and pathways. *Journal of Geophysical Research*, *99*(C6), 12,319–12,341. https://doi.org/10.1029/94jc00530

Falina, A., Sarafanov, A., Mercier, H., Lherminier, P., Sokov, A., & Daniault, N. (2012). On the Cascading of Dense Shelf Waters in the Irminger Sea. *Journal of Physical Oceanography*, *42*(12), 2254–2267. https://doi.org/10.1175/jpo-d-12-012.1

Fan, X., Send, U., Testor, P., Karstensen, J., & Lherminier, P. (2013). Observations of Irminger Sea Anticyclonic Eddies. *Journal of Physical Oceanography*, *43*(4), 805–823. https://doi.org/10.1175/jpo-d-11-0155.1

Fischer, J., Karstensen, J., Zantopp, R., Visbeck, M., Biastoch, A., Behrens, E., et al. (2015). Intra-seasonal variability of the DWBC in the western subpolar North Atlantic. *Progress in Oceanography*, *132*, 233–249. https://doi.org/10.1016/j.pocean.2014.04.002

Holliday, N. P., Bacon, S., Allen, J., & McDonagh, E. L. (2009). Circulation and transport in the western boundary currents at Cape Farewell, Greenland. *Journal of Physical Oceanography*, *39*(8), 1854–1870. https://doi.org/10.1175/2009jpo4160.1

Holliday, N. P., Bacon, S., Cunningham, S. A., Gary, S. F., Karstensen, J., King, B. A., et al. (2018). Subpolar North Atlantic overturning and gyre-scale circulation in the summers of 2014 and 2016. *Journal of Geophysical Research: Oceans*, *123*, 4538–4559. https://doi.org/10.1029/2018jc013841

Holliday, N. P., Meyer, A., Bacon, S., Alderson, S. G., & de Cuevas, B. (2007). Retroflection of part of the east Greenland current at Cape Farewell. *Geophysical Research Letters*, *34*, L07609. https://doi.org/10.1029/2006GL029085

Intergovernmental Panel on Climate Change (2013). In T. F. Stocker, D. Qin, G.-K. Plattner, M. Tignor, S. K. Allen, J. Boschung, A. Nauels, Y. Xia, V. Bex, & P. M. Midgley (Eds.), *Climate Change 2013: The physical basis. Contribution of Working Group I to the Fifth Assessment Report of the Intergovernment Panel on Climate Change*, (p. 1535). Cambridge, United Kingdom and New York, NY, USA: Cambridge University Press.

Jochumsen, K., Moritz, M., Nunes, N., Quadfasel, D., Larsen, K. M. H., Hansen, B., et al. (2017). Revised transport estimates of the Denmark Strait overflow. *Journal of Geophysical Research: Oceans*, *122*, 3434–3450. https://doi.org/10.1002/2017jc012803

Johnson, G. C. (2008). Quantifying Antarctic Bottom Water and North Atlantic Deep Water volumes. *Journal of Geophysical Research-Oceans*, *113*, C05027. https://doi.org/10.1029/2007JC004477

de Jong, M. F., Oltmanns, M., Karstensen, J., & de Steur, L. (2018). Deep Convection in the Irminger Sea Observed with a Dense Mooring Array. *Oceanography*, *31*(1), 50–59. https://doi.org/10.5670/oceanog.2018.109

Jungclaus, J. H., Hauser, J., & Kase, R. H. (2001). Cyclogenesis in the Denmark Strait overflow plume. *Journal of Physical Oceanography*, *31*(11), 3214–3229. https://doi.org/10.1175/1520-0485(2001)031<3214:citdso>2.0.co;2

Kase, R. H., Biastoch, A., & Stammer, D. B. (2001). On the mid-depth circulation in the Labrador and Irminger Seas. *Geophysical Research Letters*, *28*(18), 3433–3436. https://doi.org/10.1029/2001gl013192

Kieke, D., & Rhein, M. (2006). Variability of the overflow water transport in the western subpolar North Atlantic, 1950-97. *Journal of Physical Oceanography*, *36*(3), 435–456. https://doi.org/10.1175/jpo2847.1

Krauss, W. (1995). Mixing in the Irminger Sea and in the Iceland Basin. *Journal of Geophysical Research*, *100*(C6), 10851–10871. https://doi.org/10.1029/95JC00423

Krauss, W. (1996). A note on overflow eddies. *Deep-Sea Research Part I-Oceanographic Research Papers*, *43*(10), 1661–1667. https://doi.org/10.1016/s0967-0637(96)00073-8

Krauss, W., & Kase, R. H. (1998). Eddy formation in the Denmark Strait overflow. *Journal of Geophysical Research*, *103*(C8), 15525–15538. https://doi.org/10.1029/98JC00785

Lavender, K. L., Davis, R. E., & Owens, W. B. (2000). Mid-depth recirculation observed in the interior Labrador and Irminger seas by direct velocity measurements. *Nature*, *407*(6800), 66–69. https://doi.org/10.1038/35024048

Le Bras, I. A., Holte, J., Holliday, N. P., & Straneo, F. (2018). Seasonality of freshwater in the East Greenland Current system from 2014 to 2016. *Journal of Geophysical Research: Oceans*, *123*, 8828–8848. https://doi.org/10.1029/2018JC014511

Le Bras, I. A., Yashayaev, I., & Toole, J. M. (2017). Tracking Labrador Sea Water property signals along the Deep Western Boundary Current. *Journal of Geophysical Research: Oceans*, *122*, 5348–5366. https://doi.org/10.1002/2017JC012921

Lherminier, P., Mercier, H., Gourcuff, C., Alvarez, M., Bacon, S., & Kermabon, C. (2007). Transports across the 2002 Greenland-Portugal Ovide section and comparison with 1997. *Journal of Geophysical Research*, *112*, C07003. https://doi.org/10.1029/2006JC003716

Lherminier, P., Mercier, H., Huck, T., Gourcuff, C., Perez, F. F., Morin, P., et al. (2010). The Atlantic Meridional Overturning Circulation and the subpolar gyre observed at the A25-OVIDE section in June 2002 and 2004. *Deep-Sea Research Part I-Oceanographic Research Papers*, *57*(11), 1374–1391. https://doi.org/10.1016/j.dsr.2010.07.009

Lozier, M. S. (2012). Overturning in the North Atlantic. *Annual Review of Marine Science*, *4*(4), 291–315. https://doi.org/10.1146/annurev-marine-120710-100740

Lozier, M. S., Bacon, S., Bower, A. S., Cunningham, S. A., de Jong, M. F., de Steur, L., et al. (2016). Overturning in the Subpolar North Atlantic Program: A new international ocean observing system. *Bulletin of the American Meteorological Society*, *98*(4), 737–752. https://doi.org/10.1175/bams-d-16-0057.1

Lozier, M. S., Li, F., Bacon, S., Bahr, F., Bower, A. S., Cunningham, S. A., et al. (2019). A sea change in our view of overturning in the subpolar North Atlantic. *Science*, *363*(6426), 516–521. https://doi.org/10.1126/science.aau6592

Macrander, A., Send, U., Valdimarsson, H., Jonsson, S., & Kase, R. H. (2005). Interannual changes in the overflow from the Nordic Seas into the Atlantic Ocean through Denmark Strait. *Geophysical Research Letters*, *32*, L06606. https://doi.org/10.1029/2004GL021463

Marshall, J., & Schott, F. (1999). Open-ocean convection: Observations, theory, and models. *Reviews of Geophysics*, *37*(1), 1–64. https://doi.org/10.1029/98rg02739

McCarthy, G. D., Smeed, D. A., Johns, W. E., Frajka-Williams, E., Moat, B. I., Rayner, D., et al. (2015). Measuring the Atlantic Meridional Overturning Circulation at 26°N. *Progress in Oceanography*, *130*, 91–111. https://doi.org/10.1016/j.pocean.2014.10.006

Mertens, C., Rhein, M., Walter, M., Boning, C. W., Behrens, E., Kieke, D., et al. (2014). Circulation and transports in the Newfoundland Basin, western subpolar North Atlantic. *Journal of Geophysical Research: Oceans*, *119*, 7772–7793. https://doi.org/10.1002/2014jc010019

Nelder, J. A., & Mead, R. (1965). A simplex method for functional minimization. *Computing Journal*, *7*, 308–313. https://doi.org/10.1093/comjnl/7.4.308

Østerhus, S., Sherwin, T., Quadfasel, D., & Hansen, B. (2008). The overflow transport east of Iceland. In R. R. Dickson, J. Meincke, & P. Rhines (Eds.), *Arctic–Subarctic Ocean Fluxes: Defining the Role of the Northern Seas in Climate*, (pp. 427–441). Dordrecht: Springer Netherlands.

Peña-Molino, B., Joyce, T. M., & Toole, J. M. (2012). Variability in the Deep Western Boundary Current: Local versus remote forcing. *Journal of Geophysical Research*, *117*, C12022. https://doi.org/10.1029/2012JC008369

Pickart, R. S., Straneo, F., & Moore, G. W. K. (2003). Is Labrador Sea Water formed in the Irminger basin? *Deep-Sea Research Part I-Oceanographic Research Papers*, *50*(1), 23–52. https://doi.org/10.1016/s0967-0637(02)00134-6

Pickart, R. S., Torres, D. J., & Fratantoni, P. S. (2005). The East Greenland Spill Jet. *Journal of Physical Oceanography*, *35*(6), 1037–1053. https://doi.org/10.1175/jpo2734.1

Rhein, M., Kieke, D., & Steinfeldt, R. (2015). Advection of North Atlantic Deep Water from the Labrador Sea to the southern hemisphere. *Journal of Geophysical Research: Oceans*, *120*, 2471–2487. https://doi.org/10.1002/2014JC010605

Sarafanov, A., Falina, A., Lherminier, P., Mercier, H., Sokov, A., & Gourcuff, C. (2010). Assessing decadal changes in the Deep Western Boundary Current absolute transport southeast of Cape Farewell, Greenland, from hydrography and altimetry. *Journal of Geophysical Research*, *115*, C11003. https://doi.org/10.1029/2009JC005811

Sarafanov, A., Falina, A., Mercier, H., Lherminier, P., & Sokov, A. (2009). Recent changes in the Greenland-Scotland overflow-derived water transport inferred from hydrographic observations in the southern Irminger Sea. *Geophysical Research Letters*, *36*, L13606. https://doi.org/10.1029/2009GL038385

Sarafanov, A., Falina, A., Mercier, H., Sokov, A., Lherminier, P., Gourcuff, C., et al. (2012). Mean full-depth summer circulation and transports at the northern periphery of the Atlantic Ocean in the 2000s. *Journal of Geophysical Research*, *117*, C01014. https://doi.org/10.1029/2011JC007572

Schott, F. A., Zantopp, R., Stramma, L., Dengler, M., Fischer, J., & Wibaux, M. (2004). Circulation and deep-water export at the western exit of the subpolar North Atlantic. *Journal of Physical Oceanography*, *34*(4), 817–843. https://doi.org/10.1175/1520-0485(2004)034<0817:cadeat>2.0.co;2

Smith, P. C. (1976). Baroclinic instability in Denmark Strait overflow. *Journal of Physical Oceanography*, *6*(3), 355–371. https://doi.org/10.1175/1520-0485(1976)006<0355:biitds>2.0.co;2

Spall, M. A., & Price, J. F. (1998). Mesoscale variability in Denmark Strait: The PV outflow hypothesis. *Journal of Physical Oceanography*, *28*(8), 1598–1623. https://doi.org/10.1175/1520-0485(1998)028<1598:mvidst>2.0.co;2

Stouffer, R. J., Yin, J., Gregory, J. M., Dixon, K. W., Spelman, M. J., Hurlin, W., et al. (2006). Investigating the causes of the response of the thermohaline circulation to past and future climate changes. *Journal of Climate*, *19*(8), 1365–1387. https://doi.org/10.1175/jcli3689.1

Straneo, F. (2006). On the connection between dense water formation, overturning, and poleward heat transport in a convective basin. *Journal of Physical Oceanography*, *36*(9), 1822–1840. https://doi.org/10.1175/jpo2932.1

Toole, J. M., Andres, M., Le Bras, I. A., Joyce, T. M., & McCartney, M. S. (2017). Moored observations of the Deep Western Boundary Current in the NW Atlantic: 2004-2014. *Journal of Geophysical Research: Oceans*, *122*, 7488–7505. https://doi.org/10.1002/2017JC012984

Vage, K., Pickart, R. S., Sarafanov, A., Knutsen, O., Mercier, H., Lherminier, P., et al. (2011). The Irminger Gyre: Circulation, convection, and interannual variability. *Deep-Sea Research Part I-Oceanographic Research Papers*, *58*(5), 590–614. https://doi.org/10.1016/j.dsr.2011.03.001

Zantopp, R., Fischer, J., Visbeck, M., & Karstensen, J. (2017). From interannual to decadal: 17 years of boundary current transports at the exit of the Labrador Sea. *Journal of Geophysical Research: Oceans*, *122*, 1724–1748. https://doi.org/10.1002/2016jc012271